Bachelor Thesis

Video-based and interference-free axial force detection and analysis for optical tweezers

Sebastian Knust

Experimental Biophysics and Applied Nanosciences
Faculty of Physics
Bielefeld University

sknust@physik.uni-bielefeld.de

November 26, 2012

Academic Advisor: Dr. Andy Sischka
Head of Group: Prof. Dr. Dario Anselmetti

Acknowledgements

I would like to thank a couple of people: Prof. Dario Anselmetti for allowing me to write this thesis in his workgroup, Dr. Andy Sischka for the great advise and supervision as well as the introduction to optical tweezers, André Spiering for the help with experimental difficulties, for experimental data and advise, and Christoph Pelargus for technical advice and regular discussions.
I would also like to thank the whole group of D1 for a great atmosphere, especially my former and current office co-workers: Susan Hajisamo, Armin Grundmann, Daniel Droste, Mirjam Schulz, Roland Hillmann and Tamara Münnich.
I would also like to express my thanks to two people outside the workgroup: Fabian Czerwinski, PhD. from Princeton University for introducing me to Allan variance at the DPG spring meeting 2012, and Franziska Neugebauer for an outside look.
Finally, I gratefully acknowledge financial support from the Wilhelm and Else-Heraeus Stiftung and from the Deutsche Forschungsgemeinschaft within the Collaborative Research Center (SFB) 613.

Contents

1. Physical fundamentals **6**
- 1.1. Optical Trapping . . . 6
  - 1.1.1. Gaussian optics . . . 6
  - 1.1.2. 2D optical traps . . . 7
  - 1.1.3. 3D optical traps . . . 9
- 1.2. Force analysis at optical tweezers . . . 11
- 1.3. DNA . . . 13

2. Video-based axial force analysis **15**
- 2.1. Basic concept . . . 15
- 2.2. Edge detection . . . 15
- 2.3. Bead size detection . . . 18
- 2.4. Conversion from camera to absolute values . . . 18
- 2.5. Implementation of data analysis . . . 20

3. Experimental setup **22**
- 3.1. Original setup . . . 22
- 3.2. Changes for video-based force analysis . . . 22

4. Calibration protocols **28**
- 4.1. Calibration via Stokes' Law . . . 28
- 4.2. Analysis of the Power Spectral Density (PSD) . . . 31
  - 4.2.1. Fourier Transformation . . . 31
  - 4.2.2. Allan Variance . . . 34

5. Measurements and Results **36**
- 5.1. Interference effects and the bead size . . . 36
  - 5.1.1. Interference magnitude for different bead sizes . . . 36
  - 5.1.2. Determination of the optimal bead size . . . 38
- 5.2. Controlled translocation of DNA through solid state nanopores . . . 39

6. Conclusions **41**

7. Outlook **42**

A. Bibliography **43**

B. Appended publication **45**

C. Declaration of own work **53**

Introduction

Optical tweezers, which allow the catching of appropriately sized particles, have become a standard method for single molecule spectroscopy. In conjunction with DNA, optical tweezers are usually employed for stretching experiments, with the DNA being attached to a microbead on each end. Such an experimental setup is available in Bielefeld as well.

Another, much less widespread possibility to use optical tweezers in conjunction with DNA is the analysis of controlled translocation of the DNA through nanopores under various conditions. For this, the DNA is attached on one side to a microbead, which can be optically trapped. Then, the microbead with the attached DNA is brought into the vicinity of a nanopore with an applied voltage, leading to a threading in of the DNA. By varying the distance between between bead and nanopore, the DNA translocates the nanopore in a controlled manner. For quantitative analysis, the force applied to the microbead is measured.

In this bachelor thesis, I present a new, video-based method for measuring this axial force. As will be seen, the method is not limited to axial force analysis but can be adapted to measure forces in any of the three directions with minimal changes.

In the first chapter, I will outline the physical fundamentals of optical tweezers and DNA. In the second chapter, I will present the basic concept and ideas of video-based force analysis and discuss the implementation in the existing LabVIEW software used for controlling the experiment. The third chapter explains the original setup used with backscattered light based force analysis as well as the changes required to enable video-based force analysis. The forth chapter covers the calibration protocols for the setup. In the fifth chapter, I will present the various measurements performed with both backscattered light and video-based force analysis. The last two chapters are dedicated to the conclusions obtained from our measurements as well as an outlook for this experimental setup.

The contents of this thesis also led to the publication of an article[1] in *Review of Scientific Instruments*. It can be found at the end of the thesis together with a description of my specific contributions.

1. Physical fundamentals

1.1. Optical Trapping

1.1.1. Gaussian optics

Light, being an electromagnetic wave, is subject to the Maxwell equations, from which the wave equation (also known as the d'Alembert equation) 1.1 describing a scalar function $u(\boldsymbol{x}, t)$ can be derived:

$$\frac{\partial^2 u}{\partial t^2} = c^2 \nabla^2 u \tag{1.1}$$

c in this equation is a constant that happens to be the local speed of light $c = c_0/n$. Writing the wave equation for an euclidean coordinate system for the light field strength E yields

$$\left(\frac{\partial^2}{\partial x^2} + \frac{\partial^2}{\partial y^2} + \frac{\partial^2}{\partial z^2} - \frac{1}{c^2}\frac{\partial^2}{\partial t^2} \right) E = 0 \tag{1.2}$$

There are of course many solutions for this partial differential equation[2]. The most primitive one is the plane wave moving in e.g. z direction:

$$E(z,t) = E_0 cos(\omega t - kz) \tag{1.3}$$

with the angular frequency ω being related to the wavenumber k by $\omega = kc$.

Another common form of solution are spherical waves, who's field strength depends on the distance r from the origin of the wave. They are described by:

$$E(r,t) = \frac{A}{r} \exp\left(-i(kr - \omega t)\right) \tag{1.4}$$

Assuming the wave is centred at the centre of the coordinate system, it is obvious that $r = \sqrt{x^2 + y^2 + z^2}$.

Let us however assume that it is not centred in the coordinate system, but rather at the complex location $(0, 0, -iz_R)$ with $z_R \in \mathbb{R}$. Introducing $q := z + iz_R$ and using the notation of a cylindrical coordinate system with $r = \sqrt{x^2 + y^2}$ then leads to the form

$$E(r,z,t) = \frac{A}{\sqrt{q^2 + r^2}} \exp\left(-i\left(k\sqrt{q^2 + r^2} - \omega t\right)\right) \tag{1.5}$$

As we are only interested in the beam near the axis, the paraxial approximation $r \ll |q|$ holds true, which allows us to simplify the equation to

$$E(r,z,t) \approx \frac{B}{q} \exp\left(-i\frac{kr^2}{2q}\right) \exp\left(i(\omega t - kz)\right) \tag{1.6}$$

with $B = A\exp(kz_R)$ being – just like A – an undetermined amplitude.

We can now separate the real and imaginary part of $1/q$, which yields

$$\frac{1}{q(z)} = \frac{z - iz_R}{z^2 + z_R^2} = \frac{1}{R(z)} - i\frac{2}{kw^2(z)} \tag{1.7}$$

Here, $w(z)$ (not to be confused with ω) denotes the beam width, which stands in direct relation to the imaginary centre of the spherical wave described by z_R:

$$w(z) = \sqrt{\frac{2z_R}{k}}\sqrt{1 + \frac{z^2}{z_R^2}} \tag{1.8}$$

The radius of curvature of the wavefronts $R(z)$ depends on z_R too:

$$R(z) = z + \frac{z_R^2}{z} \tag{1.9}$$

Inserting equation 1.7 into equation 1.5 gives the most common description of a Gaussian beam, which is a paraxially approximative solution of the wave equation:

$$E(r, z, t) \approx \frac{B}{q}\exp\left(-\frac{r^2}{w^2(z)}\right)\exp\left(-i\frac{kr^2}{2R(z)}\right)\exp(i(\omega t - kz)) \tag{1.10}$$

The intensity profile of a Gaussian beam is a Gaussian, described by

$$I = I_{\max}\exp\left(\frac{-2r^2}{w^2(z)}\right) \tag{1.11}$$

The Gaussian beam is of essential importance in the field of optical tweezers as it describes the fundamental transversal mode TEM_{00} of many lasers.

1.1.2. 2D optical traps

The first observation of two-dimensional optical traps by Arthur Ashkin[3] in 1970 was motivated by the idea that the accelleration by radiation pressure of a laser targeted onto a small sphere with a size in the order of magnitude of the wavelength should be noticeable due to the small mass of the particle. For example, assuming an efficiency of $Q = 10\,\%$, a spherical particle with radius $r = 1.5\,\mu\text{m}$ and a density of $\rho = 1000\,\text{kg/m}^3$ suspended in water ($n = 1.33$) targeted by a 1 W Nd:YAG-Laser ($\lambda = 1064\,\text{nm}$) would be object to a force[4] of $F = nQP/c = 4.44 \times 10^{-10}\,\text{N}$, resulting in an acceleration of $a = F/m = 3.14 \times 10^4\,\text{m/s}^2$, about 3200 times the gravitational acceleration.

Two effects are important to the description of optical traps in the Mie regime ($2r \gg \lambda$), which is still valid for our experiments: Refraction and Reflection. Fig. 1.1 shows the basic effects for a polystyrene (PS) bead suspended in water. Symmetrically to the light's axis, the refraction induces forces away from the centre and slightly in the direction of the light, resulting in axial but no radial force. The much weaker forces

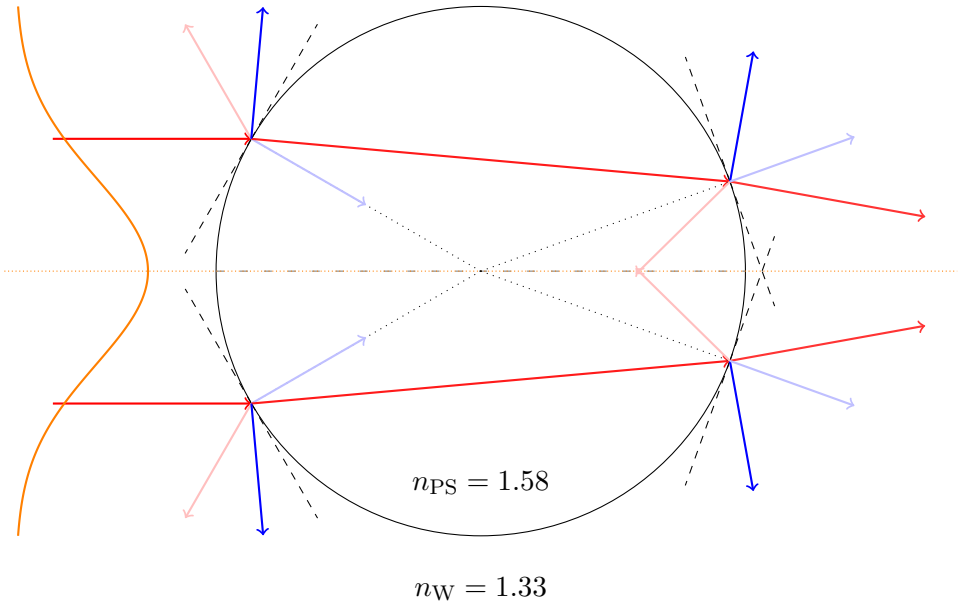

Fig. 1.1.: Light paths (red) and resulting forces (blue) for refraction (saturated) and reflection (pale) at a polystyrene bead suspended in water. Arrows indicate direction, not strength

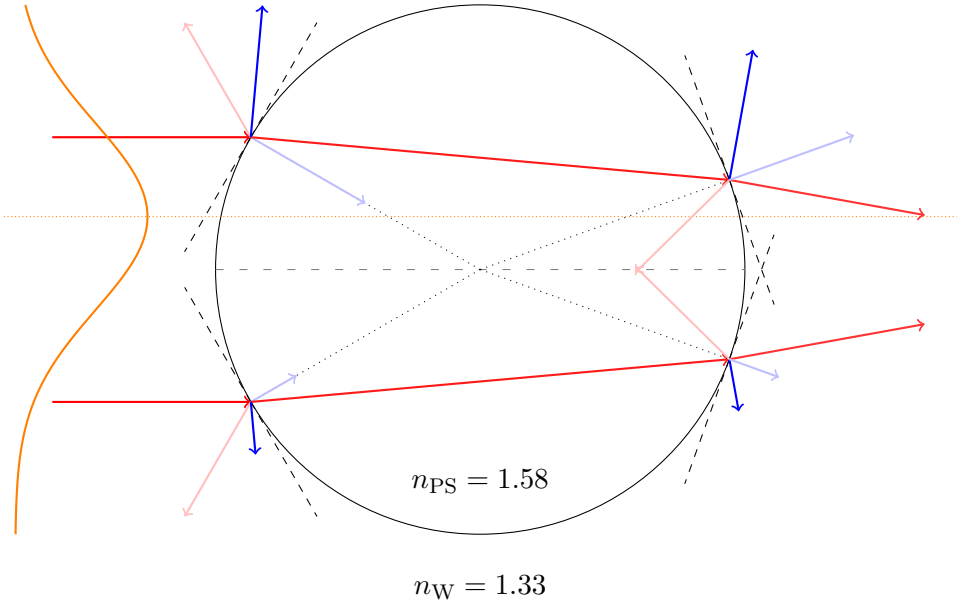

Fig. 1.2.: Light paths (red) and resulting forces (blue) for refraction (saturated) and reflection (pale) at a polystyrene bead suspended in water. Arrows indicate direction, relative blue arrow size in same saturation indicates strength

induced by reflection also point in the direction of the beam and produce no radial force.

If the beam hitting the bead is a Gaussian beam, the effects depend upon the position of the bead in the beam. If the bead is radially centred inside the beam, the intensity of the rays is symmetrical to the centre axis of the bead and the previous description holds true.

If however the bead is not centred inside the beam, the induced forces at the half nearer to the beam centre are stronger then the ones at the other half, as indicated in fig. 1.2. As the forces induced by refraction point away from the centre axis of the bead, it is pulled into the centre of the Gaussian beam, where again any displacement is counteracted with a force.

1.1.3. 3D optical traps

The problem with these two-dimensional traps is that the bead is always pushed in the direction of the propagating light by the classical *radiation pressure*. There are two ways to cope with this problem using only slightly focused Gaussian beams.

One possibility, the so-called *optical levitation*, is to use gravity as a counteracting force[5], which needs the beam to be pointing upwards. The disadvantages of this method are that it relies on gravity counteracting the radiation pressure, thus limiting the versatility of the setup as the beam always has to point upwards (and strong enough gravity has to be present) and that it only works for relatively large and therefore heavy particles (Ashkin's paper describes experiments on glass beads with 15 µm to 25 µm diameter).

Another possibility is to use two opposing beams forming a stable optical well between their beam waists, where beads are trapped. This setup allows for any orientation but still limits the versatility as two sides of the sample chamber are inaccessible and the beam paths may not be interrupted.

The problems in versatility could be eliminated if we had an optical trap created by only a single beam without the need for any external forces. Such a trap was demonstrated by A. Ashkin et. al. 1986[6]. By using a tightly focused laser beam, they were able to create a trap utilizing both positive and negative radiation pressure, depending on the position of the bead in relation to the focal point of the laser beam. Let us have a look at fig. 1.3 for the working principle.

Again, we have the two effects of refraction and reflection, and again the effects caused by reflection are small enough to be disregarded. Assuming the light is coming from the left, if the bead is positioned too far to the left, the radiation pressure is positive as with the two-dimensional trap, pushing the bead to the right. If, however, the bead is located too far to the right, because of the now strongly diverging beam, the refraction forces point backwards, creating a negative radiation pressure and moving the bead to the left.

For radial bead dislocations, the two-dimensional principle works as before: The rays passing through the part of the bead farthest away from the beam centre are weaker, therefore the radial forces do not compensate each other and force the bead back into

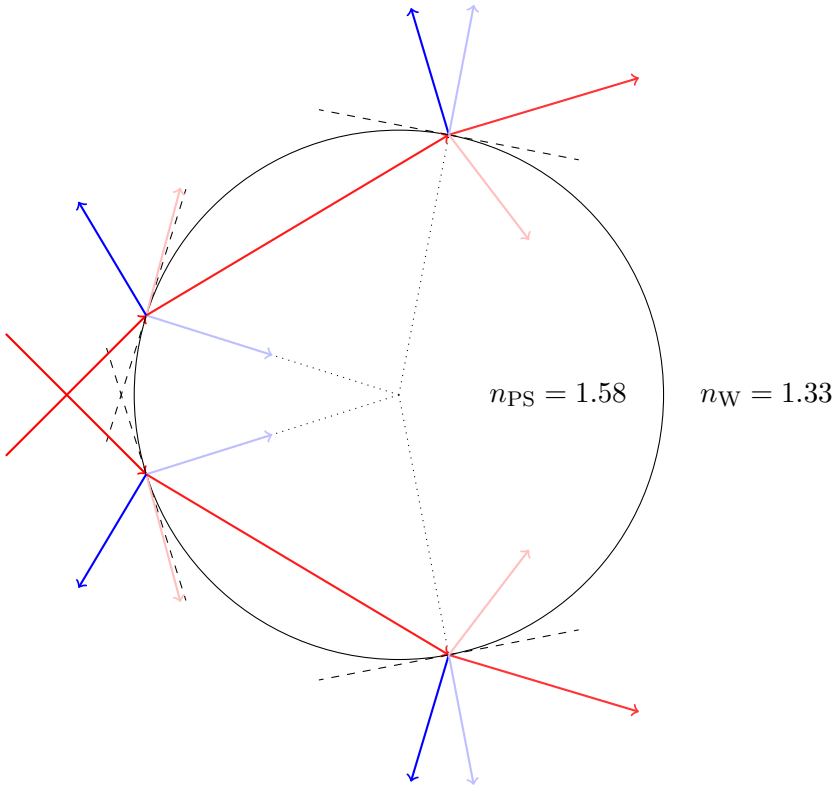

Fig. 1.3.: Light paths (red) and resulting forces (blue) for refraction (saturated) and reflection (pale) at a polystyrene bead suspended in water. Arrows indicate direction, not strength

the centre of the beam.

To sum up, a tightly focused Gaussian beam creates a three-dimensional optical trap regardless of beam orientation and independent on external effects.

1.2. Force analysis at optical tweezers

Measurement of the forces applied to the trapped bead is done by measuring the displacement of the bead from equilibrium position. It is commonly assumed that the potential of the optical trap is a harmonic one, i.e.

$$V(x, y, z) = \frac{1}{2}\left(k_x x^2 + k_y y^2 + k_z z^2\right) \tag{1.12}$$

with the displacement (x, y, z). Therefore the forces should be proportional to the displacement.

Figure 1.4 shows the numerically calculated forces acting on a bead that is axially or radially displaced. As can be seen, the assumption of forces proportional to the displacement holds true for smaller displacements ($|x|, |y| \leq 0.3\,r, |z| \leq 0.6\,r$) especially for axial displacement.

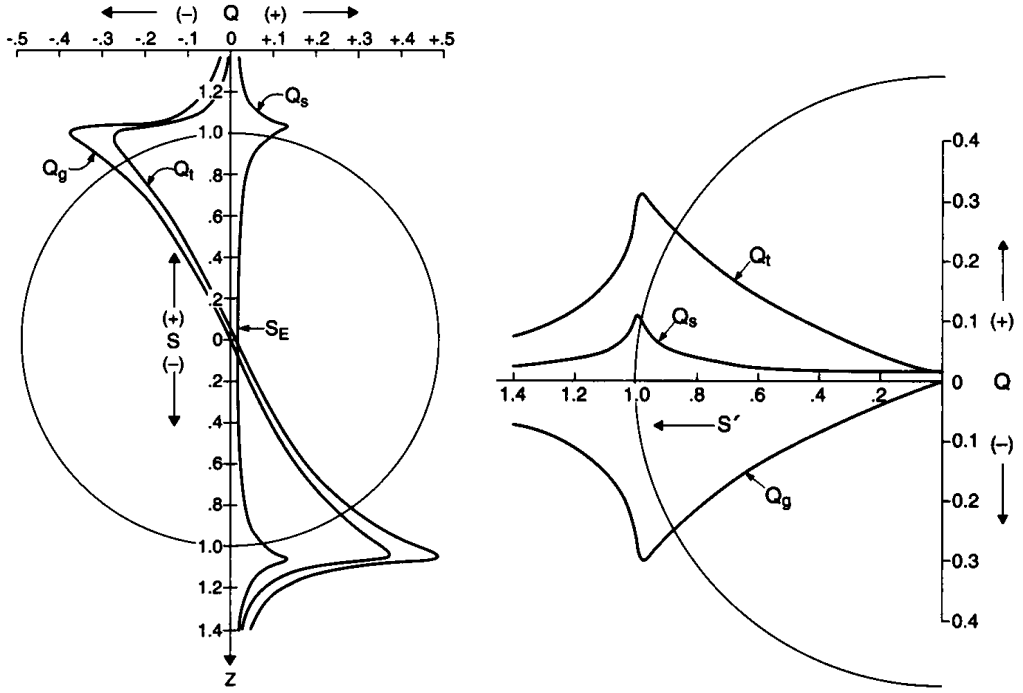

(a) Axial displacement

(b) Radial displacement

Fig. 1.4.: Gradient, scattering and total force coefficients Q_g, Q_s, Q_t (for $F = nQP/c$) at a bead with relative index of refraction $n_{\text{Bead}}/n_{\text{Fluid}} = 1.2$ as calculated by Ashkin [4]

We therefore only need to detect the displacement of the bead and convert this to a force signal. The conversion is done with various calibration protocols, which will be discussed in section 4. For the displacement detection, there are two commonly employed methods for *radial* displacements.

On the one hand, there is the possibility to analyse the forward-scattered light of the bead, as shown first by Denk and Webb [7]. The forwards-scattered beam is projected onto a four-quadrant photodiode or a linear detector, if one dimension is sufficient. As the beads is displaced to one side, the beam is deflected to the same side.

This method, however, limits the versatility of the setup as it again requires some apparatus opposite the incoming trapping beam. Backscattered light is deflected likewise by a displaced bead, however the bead's reflectivity is very low, especially since Nd:YAG lasers with $\lambda = 1064\,\mathrm{nm}$ and thus in the infrared are commonly used. One might try to add a second laser in the visible spectrum to detect the displacement, however this is very difficult to calibrate, as both beams must overlap exactly[8].

The way out is to use the polarisation of the light, as first introduced by Carter et al. [9] and incorporated into the Bielefeld setup a year later, as described in [10]. The p-polarised beam from the laser passes a quarter-wave-plate before being focused onto the trapping object. The quarter-wave-plate transforms the light into right-circular polarised light, which is left-circular polarised after being backscattered. The quarter-wave-plate transforms it into s-polarised light, which can be reflected out of the beam by a polarising beam splitter cube. This way, almost no intensity is lost, allowing for measurements on the backscattered light without a second detector laser.

On the other hand, one might employ video-based analysis. The detection of the position of a particle is a relatively trivial task, with first publications ranging back as far as 1995[11]. Until recently however, video cameras have been too slow compared to analogue detection: typically 25 Hz frame rate for PAL vs. acquisition at several dozen kHz for photodiodes. With the advent of high-speed CCD and especially CMOS cameras (which allow for easily and arbitrary reduced regions of interest), higher frame rates are achievable[12,13], but there are still some problems, especially concerning lighting, storage and post-processing speed.

Despite these problems, video-based analysis is becoming increasingly popular due to its versatility. It allows for tracking multiple beads simultaneously and is quite easy to set up and calibrate.

For *axial* displacement detection, the situation is different, as photodetectors are used almost exclusively. For the forward-scattered light, the description is rather complicated, as a Gaussian beam is subject to the so-called *Gouy phase shift* at its beam waist (which cannot be derivated from the spherical wave with the paraxial approximation as described in section 1.1.1). A particle near the beam waists changes this phase shift and therefore induces an interference between the scattered and unscattered wave. This phenomenon is described in detail in [14].

For backscattered light using the polarisation via the quarter-wave-plate as described above, the situation is easier. In this case, the axial displacement is simply linear to the backscattered light's intensity. However, it suffers from interference effects[8,10] and only works for certain specific bead sizes, as described in detail in section 5.1.

In this thesis, I introduce a method for video-based determination of the axial displacement by measuring the apparent size of the trapped bead, which will be described in detail in the next chapter.

1.3. DNA

Desoxyribonucleic acid is one of the most well known polymer molecules in nature. It is a polymer of nucleotides, each made of the sugar 2-deoxyribose which are joined by posphate groups forming phosphodiester bonds between the 5'- and 3'-C atom of two adjacent sugars. Attached to the 1'-C atom is the nitrogen atom of a base, one of adenine (A), cytosine (C), guanine (G) and thymine (T).

Two pairs of anti-parallel nucleotide strands are forming the double-helical dsDNA. Both strands are held together by hydrogen bonds, where A only binds to T and G only to C. Therefore, the two strands are complimentary to each other.

In physiological conditions, dsDNA forms a right-winded double helix called B-DNA. In this form, neighbouring base pairs are distanced 0.34 nm apart from each other and turned by 35.9°. The helix has a diameter of 2.37 nm.

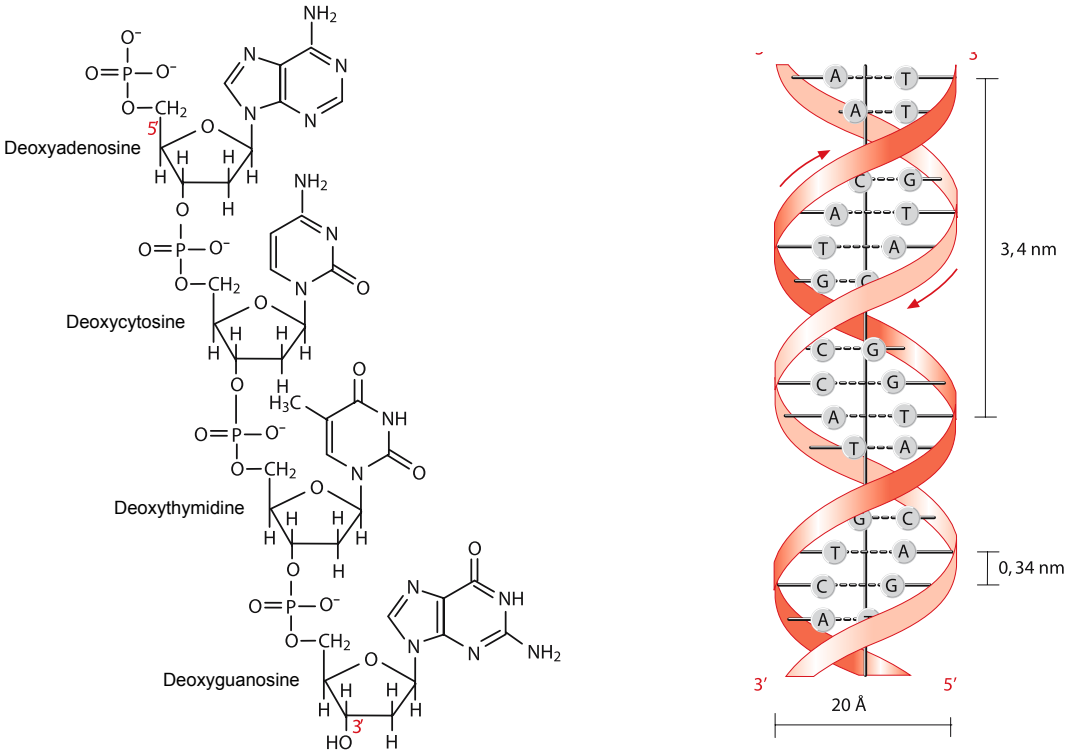

(a) The four bases in a single strand of DNA

(b) Double-helical structure of DNA

Fig. 1.5.: Components and structure of DNA, from [15]

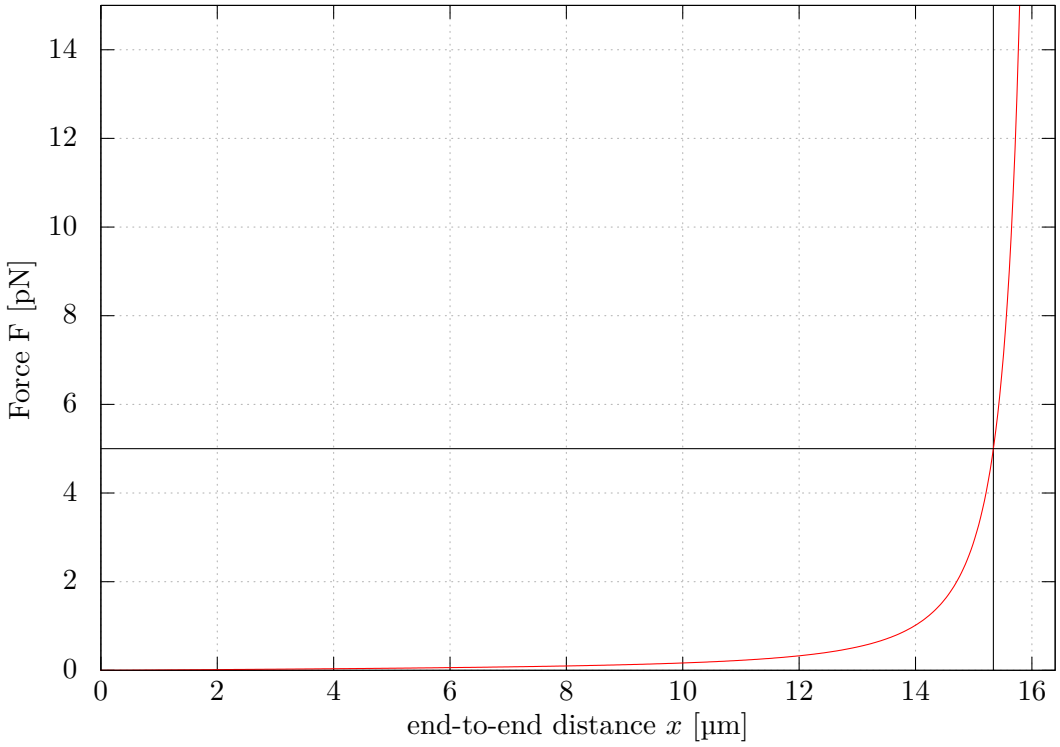

Fig. 1.6.: Forces F necessary to stretch λ DNA (contour length $L_0 = 16.4\,\mu m$) to the end-to-end distance x according to the worm-like chain model

Important for the description of DNA translocation through small nanopores is their entropic elasticity. A good theoretical description is the worm-like chain (WLC) model. It is described as a chain of segments of characteristic length ξ in the limit $\xi \to 0$, resulting in a stiff rod. The model is further described by the bending stiffness κ and the contour length L_0, with $\xi = \kappa/k_BT$. This gives the averaged quadratic end-to-end distance of:

$$\langle \bar{x}^2 \rangle = 2L_0\xi \tag{1.13}$$

In physiological conditions, a persistence length of $\xi = 50\,nm$ can be assumed.

The WLC formula can be derived from entropic considerations as an approximation[16] for the force needed to stretch the DNA to an end-to-end distance of x:

$$F = \frac{k_BT}{\xi}\left(\frac{1}{4(1-x/L_0)^2} - \frac{1}{4} + \frac{x}{L_0}\right) \tag{1.14}$$

The approximation works quite well for moderate stretching forces as applied in this work. It is shown for the dsDNA of the bacteriophage λ of *E. coli* ($L_0 = 16.4\,\mu m$) in fig. 1.6. As an example, an applied force of $F = 5\,pN$ results in an expected end-to-end distance of $x = 15.34\,\mu m$, as marked in the figure.

2. Video-based axial force analysis

2.1. Basic concept

As described before, applied forces deflect beads trapped in optical tweezers. The basic concept of video-based axial force analysis is to monitor this deflection as a change of the apparent bead size. Contrary to intuition, the thin lens formula as an approximation of the magnification M of a microscope has only negligible influence on the apparent bead size. The thin lens formula is well known as

$$M = \frac{I}{O} = \frac{i}{o} \tag{2.1}$$

The distance o between object and objective is usually in the range of 1 mm. However, typical deflections are in the range of 1 µm or smaller and therefore only one thousandth of the distance o. This would lead to a relative change in the image size I of only one thousandth as well. However, as we will see, we measure a tenfold size change.

The main observed effect is therefore not caused by the change of distance between object and objective. It is created by the changed lighting conditions and blur for a deflected bead, which leads to far greater (apparent) image size changes.

We intentionally do not analyse the visible interference pattern of the bead as this would lead to a greater region of interest and more relevant points, thus needing far more processing power. Additionally, by using only the apparent bead size, the system is more versatile for different bead materials and therefore different scattering behaviour.

2.2. Edge detection

The size of the bead is determined by searching for specific edges in the frame. I am using the built-in edge detection algorithm of the LabView Vision package at the core of the bead size detection.

Edges are large changes in the local brightness of the image, ideally discontinuities. These changes can be detected by derivation of the grey-scale intensity with respect to pixel position. Usually, the image (mathematically interpreted as a matrix of grey values) is convoluted with an operator, called a kernel. This kernel mostly fits into one of the following two categories: Either, it approximates a gradient, where the edges are located at the extreme values. Or, it approximates a Laplacian, where the edges are located at the zero crossings.

Independent of the kernel category, edge detection acts as a high pass filter, which has the unwanted side-effect of emphasizing noise in the image. Therefore, wherever feasible, direction-sensitive kernels are used which deliver good results for edges in one specific direction whilst suppressing noise in any other direction. Larger kernels also help in suppressing high frequency noise but require more computation power. It is therefore obvious that the choice of the kernel greatly influences the performance, both in respect of quantity and speed.

As I am interested in a circular edge with a – more or less – stationary centre, I do not use a convolution on the whole image. Instead, I use a gradient approach for 360 spokes along a predefined circular region of interest. Along these spokes, the extrema of the gradients and therefore the steepest rise and fall in the image intensity are determined. I then fit a circle through the middle between the rising and falling edge on each spoke. This, along with the two parameters discussed below, helps in reducing noise. Outliers are ignored if only one of the two required edges has been found. If both edges have been found, chances are high that only one of those is an outlier, thus dampening the negative effects on the overall analysis.

The kernel selection is done automatically by LabView with regard to the direction of the current spoke. However, there are two critical parameters that have to be optimized: The size of the kernel and the width of each spoke, which I will discuss shortly.

The main effect of a higher kernel size is less noise sensitivity. The larger the kernel, the more pixel are included in the calculation of the gradient for each pixel. Therefore, noise in the vicinity of the current pixel has less influence on the gradient.

The second mentioned parameter is the width of each spoke. To further reduce noise, I average over this number of edge positions one pixel parallel to the current edge.

The effects of both parameters can be seen in Fig. 2.1 (detailed look in fig. 2.2): The edge along a horizontal path from the black to the white area over the tip of the white triangle in analysed. As more perpendicular pixels are taken into account, i. e. the spoke width increases, the rising edge is detected further to the right, thus being displaced from the correct position. For spoke widths up to the double kernel size this effect is alleviated, as the kernel is directed.

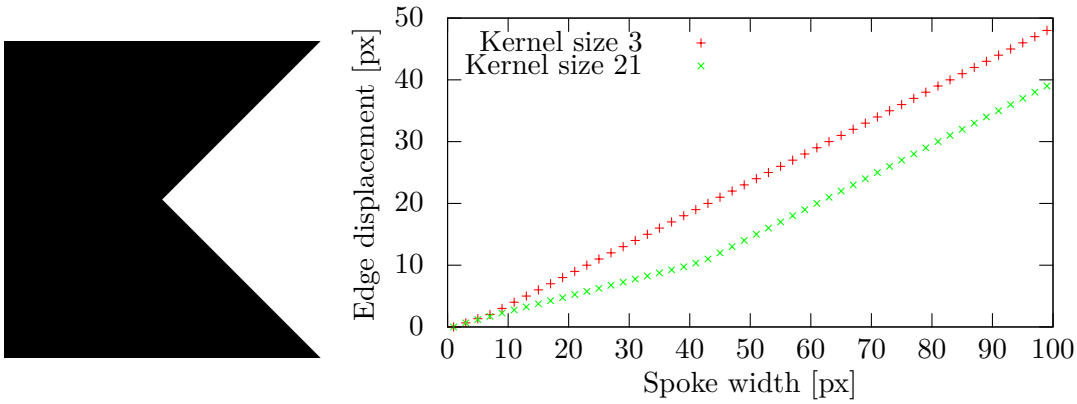

(a) Image with critical edge (b) Displacement of detected edge from the "real" position

Fig. 2.1.: Effects of kernel size and spoke width to edge detection in extreme case. The edge pointing inwards in the center of the image is detected along a horizontal line from left to right (see fig. 2.2 for magnification)

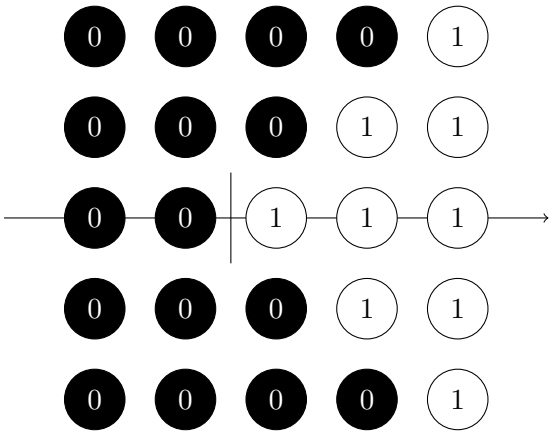

Fig. 2.2.: Detailed look at Fig. 2.1. The "real" edge position is indicated in the centre between the white and black pixel along the arrow.

2.3. Bead size detection

The process of bead size detection is illustrated in fig. 2.3 at the example of a PS bead. First, separate regions of interest for the falling and rising edges are selected manually, with the ROIs being circular and having the same centre. On demand, the ROIs can be auto tracked to compensate for drift. If this option is enabled, the centre of the ROIs is set to the last calculated centre of the circle (which can be up to six frames old, as described in the next section). Next, the strongest falling and rising edges along 360 spokes are calculated as described above. For clarity, the figure shows only every tenth search spoke. The edges are checked against a minimum edge strength selected by the user (usually set to zero, so this check always succeeds) and for correct order, i.e. whether the falling edge (red in the figure) is closer to the bead's centre then the rising edge (green). If both conditions are met, the middle position between each pair of edges is calculated. Finally, a circle (yellow) is fitted through these resulting mid-points (orange), providing position (x and y) and radius (r) of the apparent bead.

2.4. Conversion from camera to absolute values

The calculated values for position and size are in camera specific units: in pixels. The conversion of the position (let us call it ξ) can be done easily: Either by calculating the conversion factor as camera pixel size s divided by the approximate magnification factor M. In our setup, this would be:

$$\xi = \frac{s}{M} = \frac{5.6\,\mu\mathrm{m\,px^{-1}}}{60 \times 10} = 9.3\,\mathrm{nm\,px^{-1}}$$

Or one immobilises a particle on e.g. a microscope slide placed onto the piezo and moves it whilst monitoring the position with the camera. This yields a conversion factor of $\xi = (9.86 \pm 0.22)\,\mathrm{nm\,px^{-1}}$, from which the total magnification can be estimated as $M = s/\xi = 568(13)$. Of course, if one were to use this value, more detailed calibration should be done, preferable with the liquid cell instead of the microscope slide to account for different refraction indexes.

Since the size change of the bead is caused by changes in lighting condition which vary with particle material and position of the light source, it is not possible to determine a constant conversion factor β between the size change and the axial particle deflection. Instead, individual calibration is needed that should be repeated if the particle material has changed, if the particle size has changed significantly, and if the lighting has been changed, i.e. every time the liquid cell is exchanged as this inevitably leads to movement of the lighting source (see chapter 3 for details).

The calibration is carried out in the same way as the determination of the lateral conversion factor: A bead is immobilized in the vicinity of the actual force measurement position, i.e. in our case on the membrane. Then the piezo is moved in axial direction and the measured size recorded. For conversation, the following equation is used:

$$\Delta z = \beta \times \left(\frac{r}{r_{zf}(z)} - 1 \right) \tag{2.2}$$

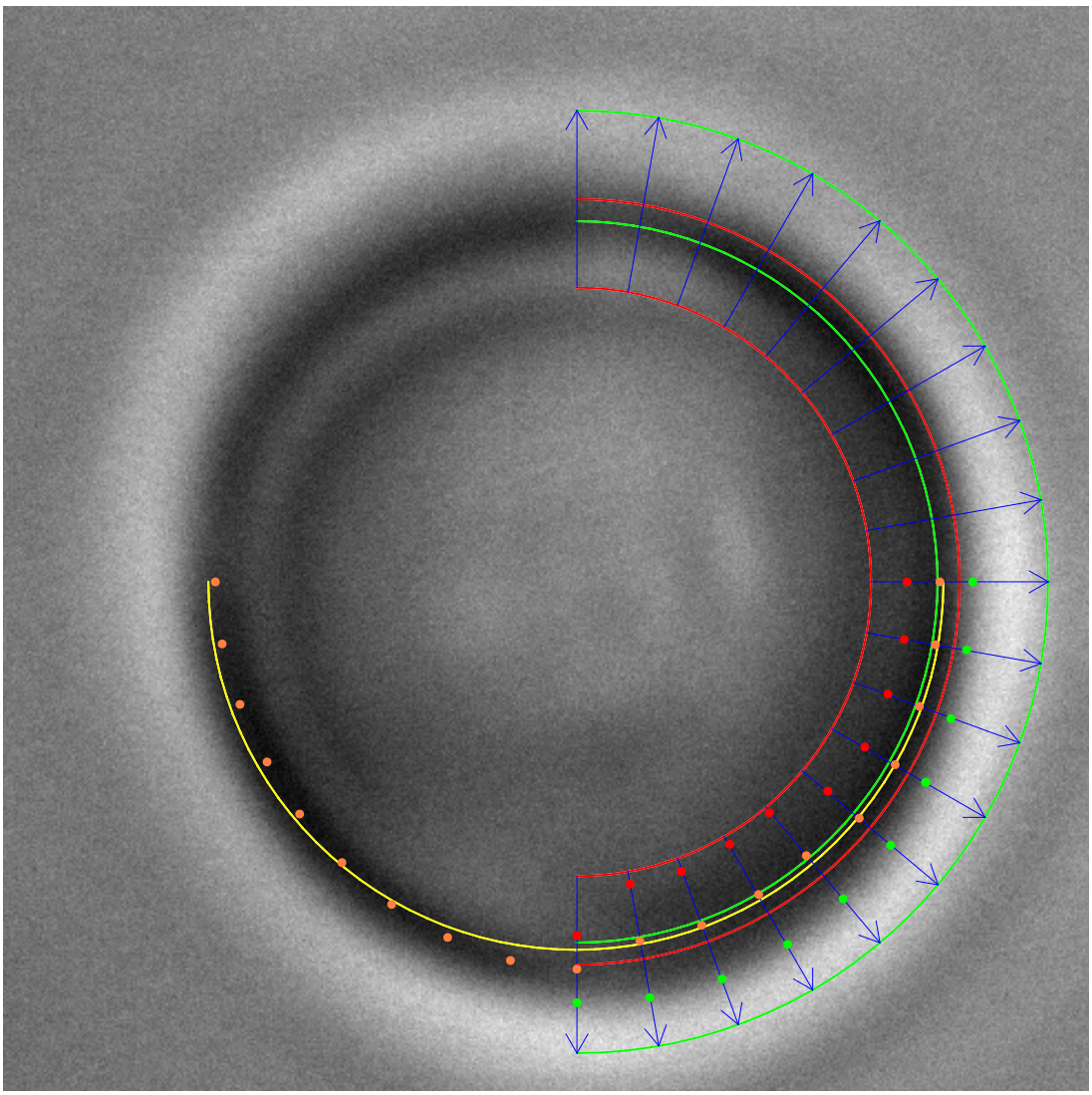

Fig. 2.3.: Still frame of a PS bead with manually selected circular region of interest for falling (red) and rising (green) edge with search spokes (blue). The red and green dots are the recognized falling and rising edges. The orange dots are the resulting mid-points between the two edges, through which the yellow circle is fitted. For clarity, only every tenth spoke with corresponding edges is shown.

Here, $r_{zf}(z)$ is the zero force radius of the bead. We noticed that in some cases the apparent bead size changes minimally with varying z position without applied force due to changed lighting conditions. Therefore, $r_{zf}(z)$ may use linear interpolation with regard to two reference measurements at different z positions.

As $F = k\Delta z$, the force is calculated as

$$F = k\beta \times \left(\frac{r}{r_{zf}(z)} - 1 \right) \tag{2.3}$$

We will later see that it is very easy to determine the factor $k\beta$, therefore the aforementioned calibration protocol is usually not employed.

2.5. Implementation of data analysis

There are two main difficulties that needed to be overcome for real-time video-based axial force analysis: The sheer amount of data, and the number of different unsynchronised data sources.

The camera delivers 123 frames per second with an image size of 492 px × 492 px at a pixel depth of 16 bits, meaning every grey-scale pixel is represented by a value between 0 and $(2^{16} - 1) = 65535$. This results in approx. 60 MB of raw image data and 88 560 edge detections that need to be processed *every second*. This is only possible by using the multithreading capabilities of modern CPUs and analysing multiple frames simultaneously. Additionally, queues should be utilized between each analysis step to prevent general slowing caused by local slowdowns.

As the camera is not the only data source and there is no synchronisation between the data sources, every value must be timestamped at acquisition. If values from two different data sources are necessary for a calculation, linear interpolation is used to approximate the value from the second source at the time the first source delivers data and vice versa.

In this setup, we have three different data sources: piezo, IO card, and camera. Therefore, every data point is interpolated two times resulting in the piezo timebase, the IO card timebase and the camera timebase. To allow for distinction, the data file streamed to disk consists of three sections: one for each timebase. In most cases however, this distinction is not necessary.

As the demands on processing power are rather large, a new computer was acquired. It offers a CPU with six cores capable of twelve simultaneous threads at a clock rate of 3.33 GHz (Intel Core i7-980). The LabView software for controlling and analysing the setup was rewritten almost completely from scratch, only a few user interface functions were reused from the previous software. LabView as the programming environment was chosen for three reasons: It's data flow model offers inherent parallelism, it is relatively easy to use for such complex tasks in contrast to classical programming languages, and it is the de-facto standard for scientific measurement and automation. As it offers all available tools to do video analysis, I discarded the idea to use a separate program like Matlab to out-source the actual video-analysis.

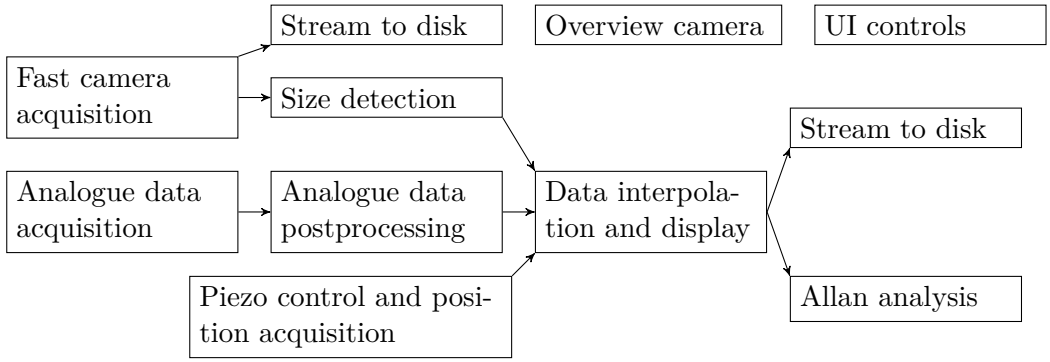

Fig. 2.4.: Structure and dependencies of the eleven main loops

Unfortunately, some drivers, notably the ones for the IO card, are only available in 32 bit versions. Therefore, even though the system is equipped with 12 GB of RAM, only 4 GB are directly accessible by the operating system and therefore the running programs.

The relevant parts of the program are contained within eleven loops as illustrated in fig. 2.4. Data acquisition from the camera and the IO card is handled in individual loops that push the data into a queue to make sure no data is lost due to slow acquisition. This is especially important for the camera acquisition, as the camera has no on-board buffer.

Likewise, streaming of the data to disk (if enabled) is done in separate loops to account for the slow disk speed. This way, if the disk cannot handle the data rate, it is simply buffered in memory without slowing down the rest of the program. However, as memory is limited, the queue would eventually become larger then the available memory, leading to loss of data. This could be counteracted by using the remaining RAM that is unusable by programs as a temporary disk and streaming target. As it is not necessary to save long video sequences, this workaround has not been used yet.

The main part of the program is the size detection. To ensure maximum performance whilst avoiding concurrency problems, I implemented it in a semi-parallel fashion. In every run of the size detection loop, six frames are dequeued and analysed. For every frame, the circular edge detection of the rising and the falling edge are running in parallel as well. Thus, all twelve threads of the CPU are utilised (usually to 90 %).

On might argue that it would be better to leave one thread dedicated to the rest of the program. However, this would lead to either the calculation of five and a half frames per cycle, which would complicate the programming enormously, or to the calculation of eleven frames per cycle, leading to unnecessary code duplication, or to the use of two threads for the remaining tasks, which would have been an overkill.

The method is only semi-parallel as the loop waits for all six frame analysis to be finished before starting again with the next six frames. The reason for not using the parallel loop execution feature of LabView is that this would have massively complicated the zero force calibration which is done in this loop as well. One would have gotten a simpler size detection loop at the cost of another loop just for this calibration.

3. Experimental setup

3.1. Original setup

The setup prior to the changes necessary for is illustrated in fig. 3.1 and described in detail in [10]. It consists of a Nd:YAG laser (LCS-DTL-322-1000[17], Laser 2000, Germany; 1064 nm, 1 W, linear polarised TEM_{00}, full divergence angle 1.6 mrad, beam diameter (1.2 ± 0.1) mm), a longpass to filter out the pumping light, a polarised beam splitter that directs the backscattered light onto a linear detector for radial and a photodetector for axial measurements, a beam expander, a central obstruction filter, a quarter-wave-plate and a dichroic mirror. Data from the linear and photodetector is acquired with a NI PCI-6036E IO card (National Instruments, TX; 16 bit, 200 kS s^{-1}). The setup is incorporated in an Axiovert 100 microscope (Zeiss, Germany). The 60× trapping objective (UPL-APO60W/IR) is a water immersion objective with a numerical aperture of 1.2. As very small electric currents are measured in nanopore experiments, the piezo stage, sample chamber and end of the illumination fibre optics are placed inside a Faraday cage.

Further incorporated are a standard b/w CCD camera for monitoring purposes, short pass filters in the visible light pass to block the IR light still transmitted by the dichroic mirror, and a KL-200 (Schott, Germany) cold light source whose light is coupled into the setup by a fibre optic. The 20 W halogen bulb delivers approximately 50 lm of light.

3.2. Changes for video-based force analysis

For video-based analysis, two main components of the system were changed. Obviously a camera was added, together with an additional magnification optics. Also, the cold light source was changed.

The camera is a Guppy Pro F-031B[18] (Allied Vision Technologies, Germany) CCD camera with a Sony IT CCD ICX618AL/AQA sensor and a 14 bit analogue-digital-converter (ADC). It was chosen for its combination of a relatively high frame rate of up to 123 fps at full resolution (656 px × 492 px) and small square pixel size of 5.6 µm. The latter simply leads to a higher resolution of objects.

Image data can be transferred in 8, 12 and 16 bit modes via Firewire.B. The maximum payload data is limited by the Firewire protocol to 524.288 Mbit s^{-1} (125 µs cycles with 8192 bytes each). Therefore, in 16 bit mode the transfer protocol limits the maximum resolution to a total of 266 406 px per frame. As for optimal compatibility the horizontal and vertical resolution should be dividable by 4, the maximum usable reso-

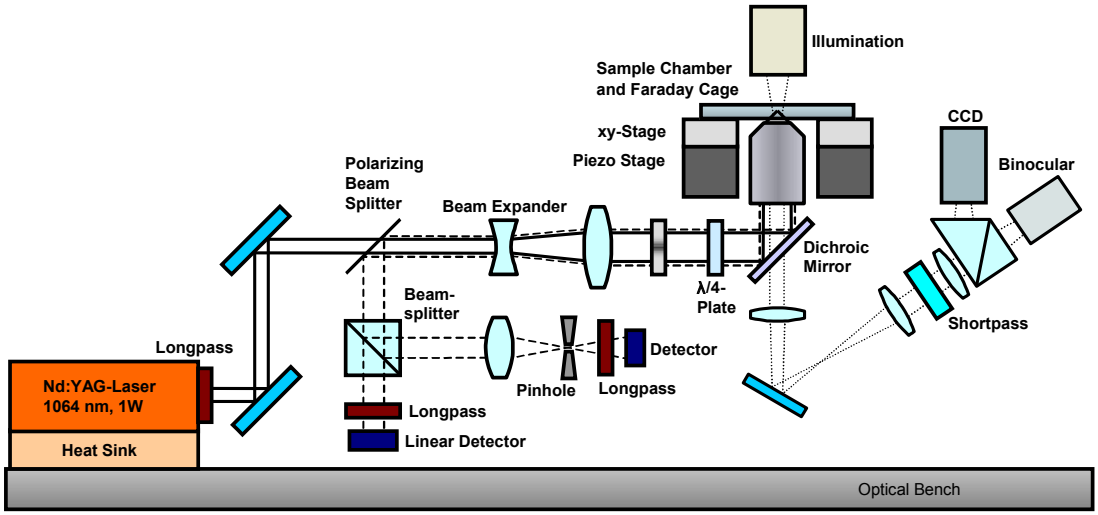

Fig. 3.1.: Experimental setup prior to the changes for video-based analysis

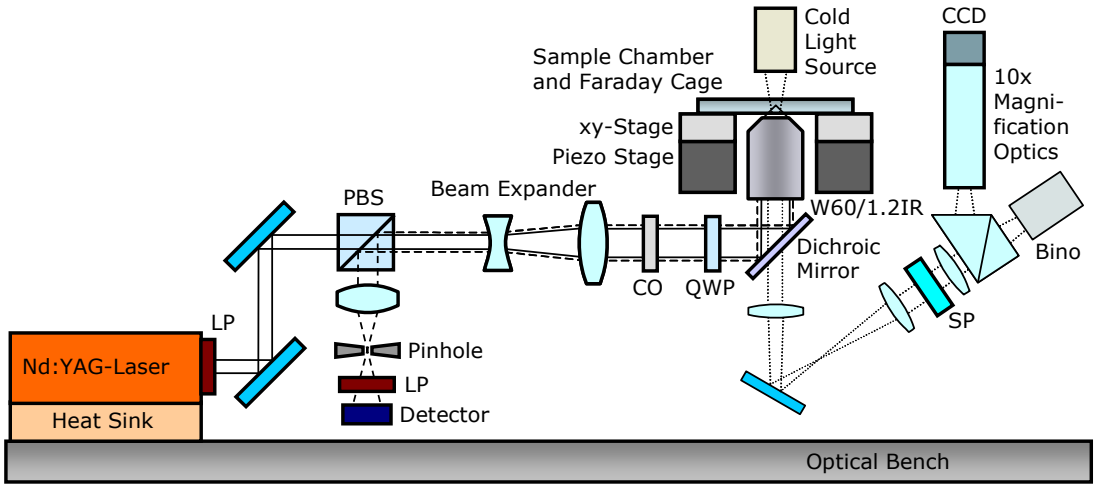

Fig. 3.2.: Experimental setup after to the changes for video-based analysis. Note that the old CCD is still incorporated in the setup and accessible by a switchable prism

lution would therefore be 540 px × 492 px. As the additional horizontal resolution is of no benefit for axial force detection, the program uses only a square region of interest of 492 px × 492 px.

In the performed measurements, a 1 % apparent bead size change equals a force of approximately 1 pN at 250 mW laser power, a typical force to be measured. Without the use of a postmagnification optics, a bead would have a diameter of about 40 px, thus a size change of 0.4 px would already be a typical force. For improved performance, the image needs to be magnified before being detected by the CCD. This is done by a custom-made magnification optics: essentially, a small telescope with a magnification factor of about 10. With it, a typical bead radius of 170 px to 180 px is achieved. With this setup, the program is able to discern 0.05 px radius changes or relative changes of 0.025 %, which would correspond to a force of 25 fN.

The CCD camera and the postmagnification pose a problem that is addressed with the change of lighting: Higher frame rates correspond to lower shutter times, therefore less time for light to hit the pixels of the CCD and therefore less image intensity. This problem is amplified by the use of magnification optics, as they further reduce the amount of light that hits the camera. Therefore, it is obvious that a high light intensity is needed.

The first try was to place the fibre directly onto the sample chamber as illustrated in fig. 3.3a. Activating the full camera gain yielded a usable image with a high amount of noise. This was sufficient to test and further develop the detection program, but not good enough for productive measurements.

Illumination with a laser in the visible spectrum would have delivered high intensities, but also the possibility to generate a second trap. Furthermore, the coupling would not have been easy and one would have to pay attention to avoid speckle patterns. For these reasons, the idea of laser illumination was not pursued any further.

As preliminary testing with a low-power halogen bulb seemed promising, the next step was to try a 2 kW halogen bulb next to the microscope with the light being inserted into the visible light path between binocular and dichroic mirror via a half-reflecting mirror. This setup would have worked as an reflecting microscope: The illuminating light is focused by the microscope optics and the reflection is analysed. Whilst coupling would have been difficult, the Osram 64789 CP/73 light bulb we used radiated with an intensity of 52 000 lm, more then a thousand times brighter then the previous cold light source.

One important problem however is the heat generated by this bulb. The light temperature is $T = 3200\,\mathrm{K}$. Using Planck's radiation law, we find for the part of light in the infrared and above:

$$p = \frac{\displaystyle\int_{800\,\mathrm{nm}}^{\infty} \frac{2\pi hc^2}{\lambda^5} \frac{1}{\exp\left(\frac{hc}{\lambda k_B T}\right) - 1} d\lambda}{\displaystyle\int_{0}^{\infty} \frac{2\pi hc^2}{\lambda^5} \frac{1}{\exp\left(\frac{hc}{\lambda k_B T}\right) - 1} d\lambda} = 82.6\,\% \tag{3.1}$$

At first, I tried to use infrared filter glasses in front of the halogen bulb. However,

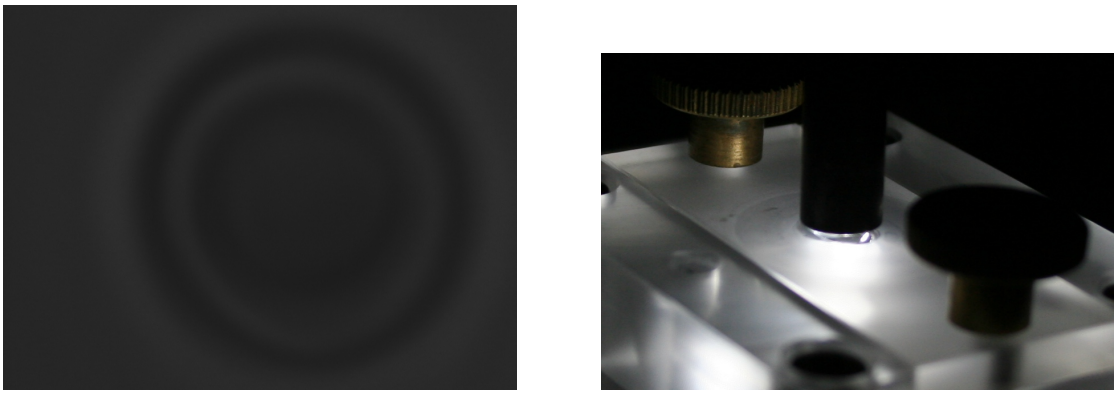

(a) KL-200 with fibre directly on top of sample chamber

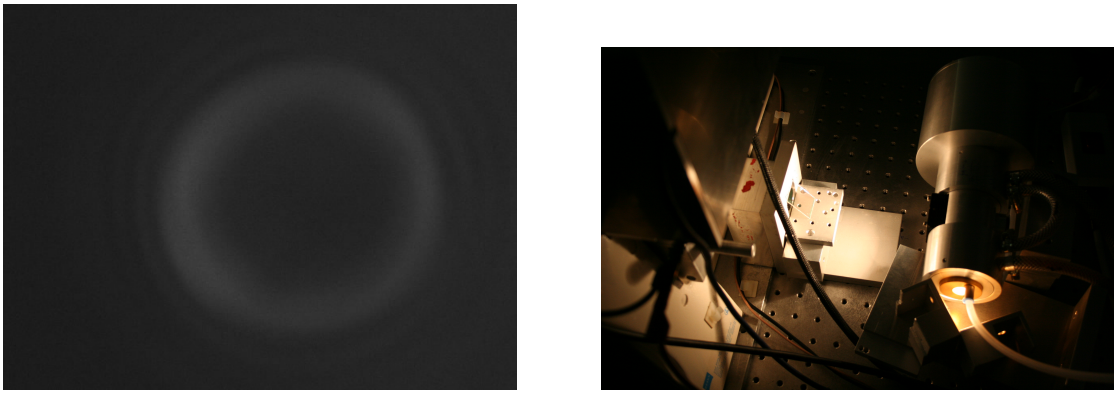

(b) 2 kW halogen bulb irradiating between binocular and dichroic mirror (image taking during daytime with ceiling lights switched on). The halogen bulb is contained in the water-cooled enclosure in the right. The IR mirror can be seen in front of the whole near the centre of the image

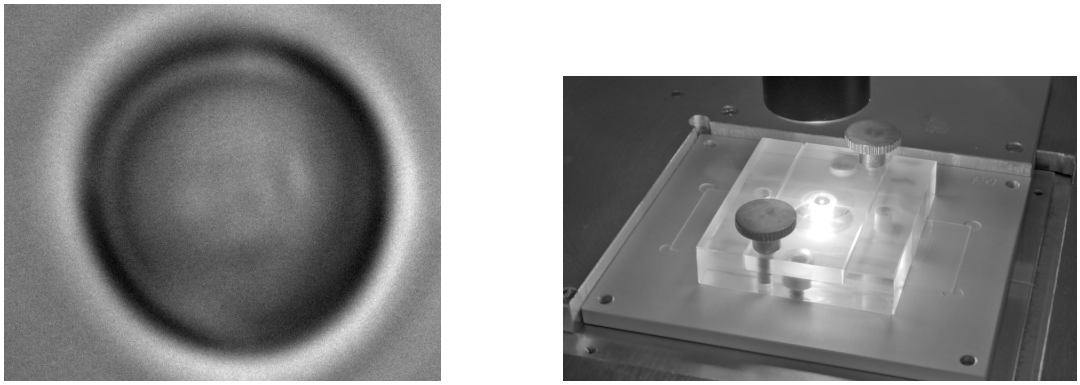

(c) KL-2000 LED with collimator focused onto sample chamber

Fig. 3.3.: Beads imaged with different lighting sources with same camera settings and corresponding lighting setups

I only succeeded in melting them. In the second try, an IR mirror was used to reflect the infrared part of the spectrum to the ceiling. This provided very good illumination with regard to the rudimentary setup. However, the edges were not sharp any more as illustrated in fig. 3.3b.

Therefore, the final setup again incorporates a cold light source but with higher power. The KL-2000 LED (Schott, Germany) consists of seven 9 W high power LEDs delivering an output of 1000 lm. To provide access for electrodes to the centre reservoir, the fibre is not placed directly onto the sample chamber. Instead, the light is focused by a collimator approx. 2 cm in front of the sample chamber onto it. This leads to a bright enough image as seen in fig. 3.3c, especially if a water droplet is placed on top of the middle reservoir. However, exchanging the sample chamber almost inevitably leads to a movement of the collimator. Additionally, as the water droplet on the middle reservoir evaporates, the lighting changes as well. Therefore, the droplet should be checked and filled up regularly and calibration should be done at least after every sample chamber change.

Sample heating by illumination can be a problem, as the sample chamber contains only a small amount of water. Biological samples are heat sensitive and the viscosity of water is strongly temperature dependent. We therefore monitored the heating process induced by the illumination with a thermographic camera, as illustrated in fig. 3.4. It showed that the sample chamber is heated up to 25 °C. At this temperature, the viscosity of water[19] is 0.8902 mPa s.

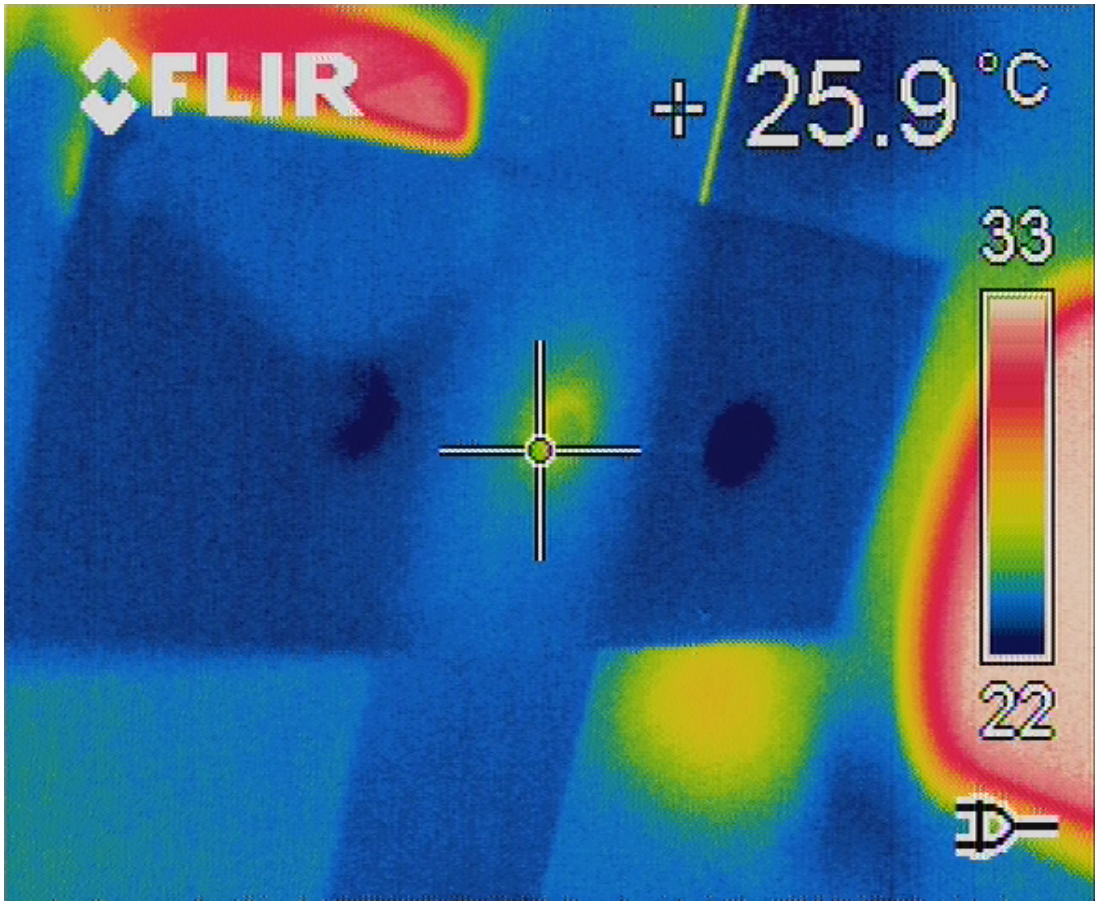

Fig. 3.4.: Thermographic image of a sample canal with two reservoirs on the sides (dark circles) and a central reservoir with chip containing membrane (marked heat spot). The collimator of the cold light source can be seen as a hot object on the right edge of the image

4. Calibration protocols

As the theoretical calculation of trapping forces of optical tweezers is unreliable – it depends on exact knowledge of trap geometry and laser power, both not constant in a real-world setup – empirical calibration protocols are necessary. There are two principal methods: One is to use Stoke's law directly and move trapped particles at a specified speed. The other is to analyse the power spectral density, usually via Fourier transformation.

4.1. Calibration via Stokes' Law

A spherical particle with radius r moving with a velocity $\boldsymbol{v}$ relative to a liquid with viscosity η is subject to Stokes' force:

$$\boldsymbol{F} = -6\pi\eta r\boldsymbol{v} \tag{4.1}$$

This equation is only valid for laminar flow, which is characterised by a Reynolds number of $Re = vr\rho/\eta \ll 100$ with the particle density ρ. For example, our typical polystyrene particles in water moving at $v = 5000\,\mu\mathrm{m\,s}^{-1}$ have a Reynolds number of[20]

$$Re = \frac{vr\rho}{\eta} = 7.5 \times 10^{-3}$$

and are therefore safely within the bounds for laminar flow.

Additional attention has to be paid for movement parallel to a surface. If the distance to the surface h is in the order of magnitude of the bead size, the drag coefficient must be adjusted[20]:

$$F = \frac{6\pi\eta r v}{1 - \frac{9}{16}(a/h) + \frac{1}{8}(a/h)^3 - \frac{45}{256}(a/h)^4 - \frac{1}{16}(a/h)^5 + \mathcal{O}((a/h)^6)} \tag{4.2}$$

Similarly, when moving the bead perpendicular to a surface, a correction factor λ with $F = 6\pi\eta r v\lambda$ is introduced, with[21]

$$\lambda = \frac{4}{3}\sinh\alpha \sum_{n=1}^{\infty} \frac{n(n+1)}{(2n-1)(2n+3)} \left(\frac{2\sinh((2n+1)\alpha) + (2n+1)\sinh 2\alpha}{4\sinh^2((n+\frac{1}{2})\alpha) - (2n+1)^2\sinh^2\alpha} - 1 \right) \tag{4.3}$$

In this equation $\alpha := \operatorname{arccosh}(h/r)$ with the bead radius r and the distance between bead centre and surface h. It is plotted in fig. 4.1 with some values highlighted in table 4.1.

For axial force calibration, one now simply measures two reference sizes for the linear zero force interpolation, moves the bead to a starting distance and moves back and

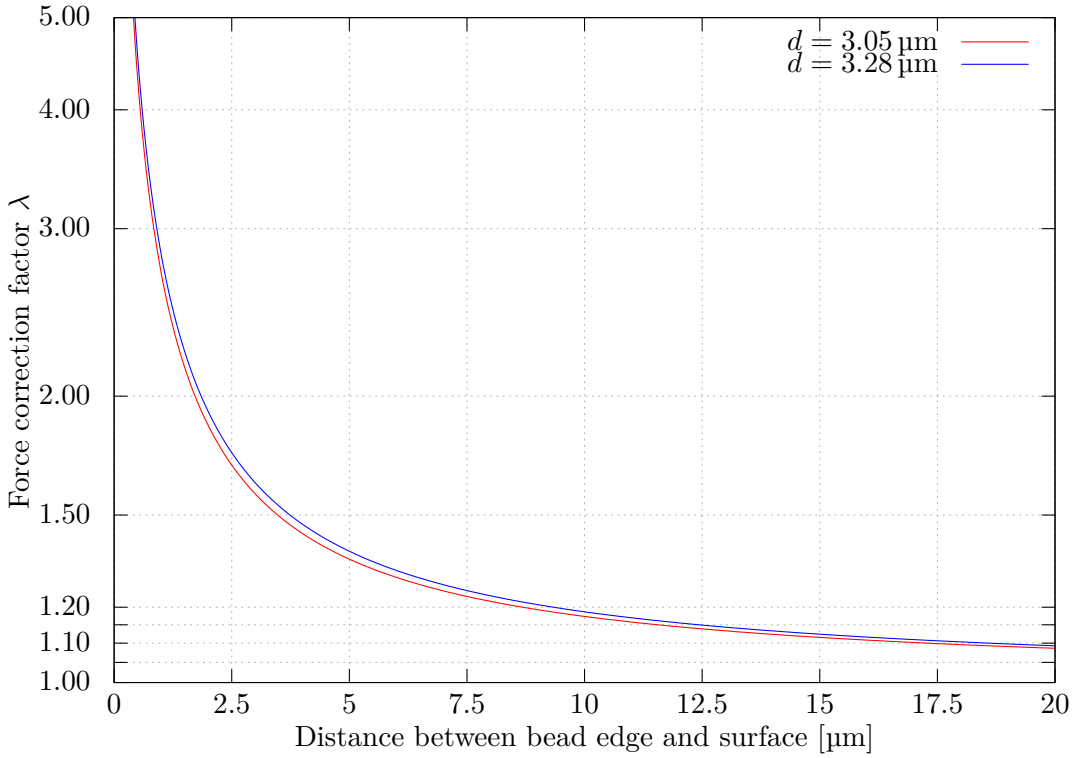

Fig. 4.1.: Correction factor for movement perpendicular to a surface for 3.05 µm and 3.28 µm beads. Values are calculated up to the 100th term with Gnuplot 4.7

z[µm]	λ (3.05 µm bead)	λ (3.28 µm bead)
0.50	4.112	3.570
1.00	2.630	2.470
2.00	1.839	1.795
5.60	1.304	1.298
10.00	1.170	1.168
15.00	1.113	1.112
20.00	1.085	1.084
11.23		1.150
11.34	1.150	
16.87		1.100
16.99	1.100	
33.77		1.050
33.89	1.050	

Table 4.1.: Correction factors for various distances z between bead and surface for 3.05 µm and 3.28 µm beads. Values are calculated up to the 100th term with Maple 12

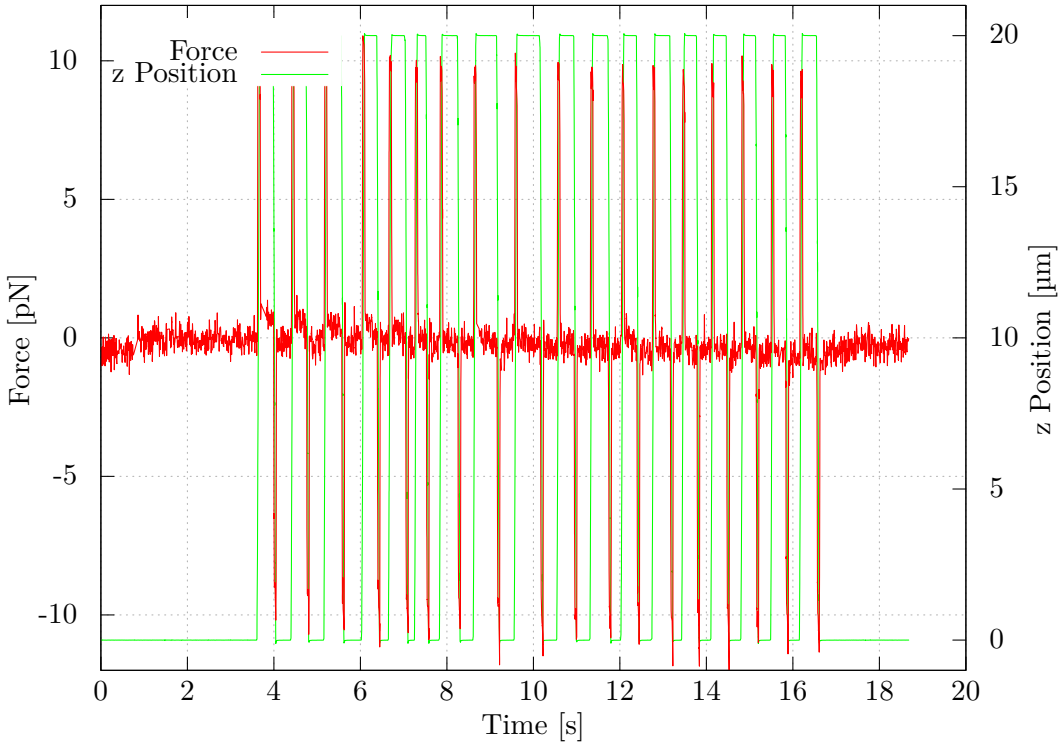

Fig. 4.2.: Example of a drag force calibration with a speed equivalent to 10 pN

forth between this point and the maximum piezo position $z = 20\,\mu m$ at a speed usually equivalent to a force of 5 pN or 10 pN, as illustrated by fig. 4.2. The conversion factor $k\beta$ is then adjusted so that the positive force spike has the correct value, either by calculating the value or by simply guessing it. As the force spike will not always have the same value due to piezo effects, dirt particles, etc. the letter method is sufficient, as long as the final value is checked with a few more movement operations, preferable at more then one speed. If the movement takes place in the vicinity of a surface (e.g. a membrane or the side of the sample cell), the above-mentioned correction factor has to be used. As the overall accuracy of this method is not very high, an average value can be used instead of the complete function.

The advantages of the Stokes method are that it is fast, intuitive and can be done online, i.e. the results are available immediately and not only after a more or less extended calculation.

The main disadvantage however is obvious: the bead needs to be moved. That gives rise to a multitude of problems. First, the movement of the bead is dangerous in the sense that it is very easy to trap another bead, dirt or air bubble which renders the currently trapped bead useless.

Another problem is that the dependency of the zero force bead size on the focus may be more complex than assumed. Also, a typical movement takes only 75 ms for 10 pN,

which means that only about nine frames are recorded during full movement. Likewise, the piezo also delivers data at a rate of about 120 Hz. As the linear interpolation gives wrong values at sudden accelerations, the first and last data point must be discarded, resulting in only seven points for which reliable data is present.

The direct dependency on the movement speed also means that we rely on correctly working piezos. Although this can be assumed and was verified recently during a repair at the manufacturer, it adds another unnecessary dependency to the calibration process.

Overall, the drag force method yields a calibration error of approximately 10 %.

4.2. Analysis of the Power Spectral Density (PSD)

In contrast to the drag force method, which relies on applied forces, the analysis of the power spectral density uses the inherent properties of the fact that the bead is trapped in a harmonic potential. The Langevin equation for a particle with friction coefficient γ is:

$$\gamma\dot{x} + kx = F(t) = \zeta(t)\sqrt{2k_BT\gamma} \tag{4.4}$$

For Brownian motion, $\zeta(t)$ is a stochastic variable with $\langle\zeta(t)\rangle = 0$ and $\langle\zeta(t)\zeta(t')\rangle = \delta(t-t')$.

The equation can be rewritten using the Stokes-Einstein equation $D = k_BT/\gamma$ as

$$\dot{x} = \frac{k}{\gamma}x + \zeta\sqrt{2D} \tag{4.5}$$

which in turn is used as the basis for all subsequent transformations.

It should of course be noted that the friction coefficient has to be adapted to the vicinity of surfaces, according to eqs. 4.2 or 4.3 for radial or axial forces.

4.2.1. Fourier Transformation

The most used method for power spectral density analysis is the Fourier transformation. Fourier transformation of eq. 4.5 yields:

$$\tilde{x}(\omega) = \frac{\sqrt{2D}}{i\omega + k/\gamma} \tag{4.6}$$

The power spectrum is therefore

$$P(\omega) = \frac{2D}{\omega^2 + (k/\gamma)^2} \tag{4.7}$$

which can be rewritten as

$$P(f) = \frac{k_BT}{2\pi^2\gamma(f^2 + f_c^2)} \tag{4.8}$$

with the corner frequency $f_c = k/2\pi\gamma$.

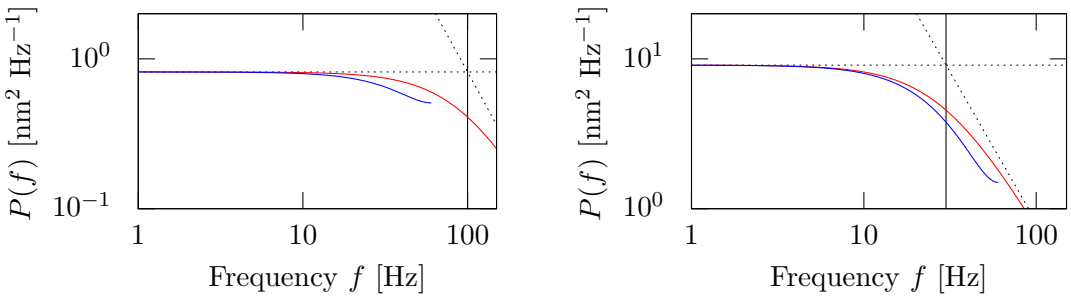

(a) $f_c = 100\,\mathrm{Hz}$ (b) $f_c = 30\,\mathrm{Hz}$

Fig. 4.3.: Exemplary differences between the PSD with (blue) and without (red) low pass correction (sampling frequency $f_s = 120\,\mathrm{Hz}$)

This form of the power spectrum assumes an infinite sampling rate. For force analysis with photodiodes that deliver sampling rates of multiple kHz, this assumption is approximated very well. For our video-based setup delivering only 123 Hz, a low pass correction must be introduced. Assuming the sampling frequency f_s is the inverse of the shutter time, this correction yields[22]:

$$P^*(f) = \frac{2k_BT\gamma}{k^3}\left(k + \frac{2\gamma f_s \sin^2\left(\frac{\pi f}{f_s}\right)\sinh\left(\frac{k}{\gamma f_s}\right)}{\cos\left(\frac{2\pi f}{f_s}\right) - \cosh\left(\frac{k}{\gamma f_s}\right)}\right) \tag{4.9}$$

The effects of the low pass correction are illustrated in fig. 4.3.

Apart from the necessary low pass correction, fourier-based PSD calibration also suffers directly from the low sampling rate, allowing only for very imprecise fits. Whilst the method is very capable for data sampled with a high frequency, it is not suited for data with low sampling rates.

Figure 4.4 shows fourier-transformed data from video-based analysis. The low pass-corrected spectrum was fitted to the data with Origin and Gnuplot with the same starting values. As can be seen in table 4.2, both programs deliver different results with gnuplot declining to give an error estimation. Just looking at the graph shows the difficulty in fitting.

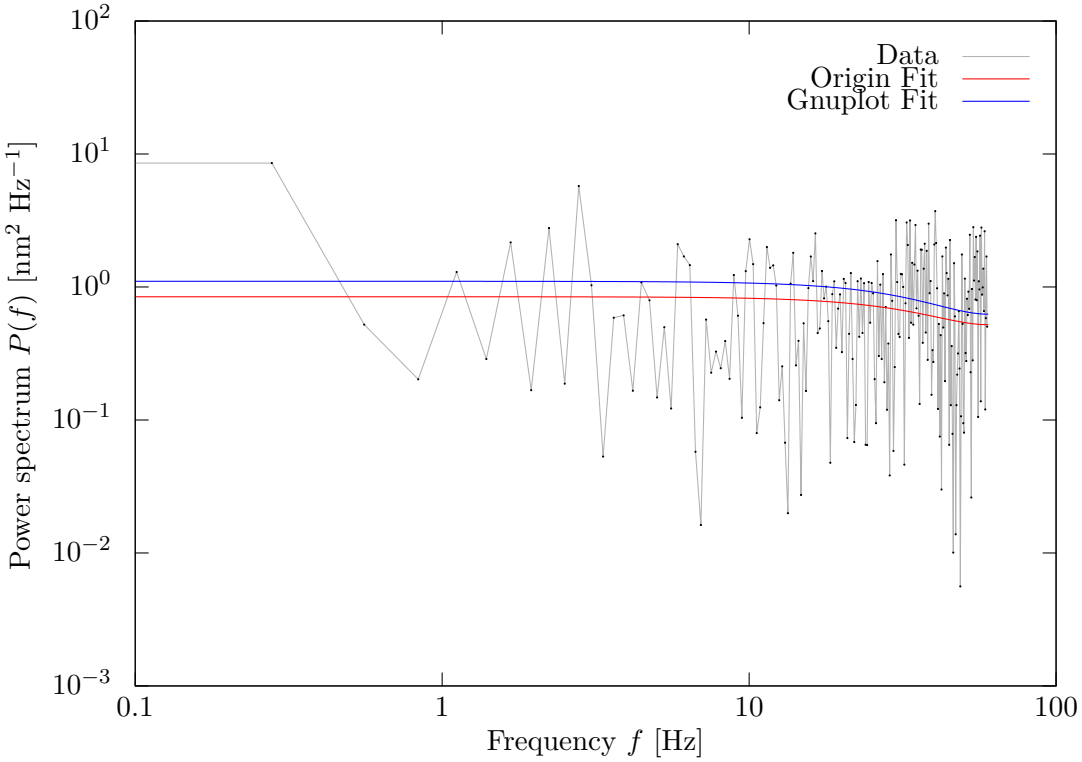

Fig. 4.4.: Example of a Lorentzian spectrum fit to fourier-transformed video-based data.

	f_c	βk
Origin	(99.4 ± 4.4) Hz	(289 ± 19) pN
Gnuplot	86.0 Hz	253 pN
Allan	(99.6 ± 0.4) Hz	(293 ± 7) pN

Table 4.2.: Fit parameters for fig. 4.4 from the fit with Gnuplot and Origin as well as results from Allan analysis

4.2.2. Allan Variance

Allan variance is a method perfectly capable of coping with low frequency signals. It is defined as half the variance of the averaged difference between two consecutive local averaged position samples:

$$\sigma_A^2(\tau) = \frac{1}{2}\left\langle (\bar{x}_{\tau,j+1} - \bar{x}_{\tau,j})^2 \right\rangle \qquad \bar{x}_{\tau,j} = \frac{1}{\tau}\int_{\tau(j-\frac{1}{2})}^{\tau(j+\frac{1}{2})} x(t)dt = \left[x * \Pi_\tau\right](j\tau) \tag{4.10}$$

Expanding this equation and using $\langle \bar{x}_\tau^2 \rangle := \langle \bar{x}_{\tau,j}^2 \rangle = \langle \bar{x}_{\tau,j+1}^2 \rangle$ due to the stationary nature of the process gives the relation to the variance and autocorrelation as:

$$\sigma_A^2(\tau) = \langle \bar{x}_\tau^2 \rangle - \langle \bar{x}_{\tau,j+1}\bar{x}_{\tau,j} \rangle \tag{4.11}$$

The Wiener-Kinchin theorem[23] can then be used to relate the Allan variance to the PSD:

$$\sigma_A^2(\tau) = \int_{-\infty}^{\infty} \frac{4\sin^4(\pi f\tau)P(f)}{(\pi f\tau)^2} df \tag{4.12}$$

which, with $P(f)$ from eq. 4.8 gives us

$$\sigma_A^2(\tau) = \frac{2k_BT\gamma}{k^2\tau}\left(1 + \frac{2\gamma}{k\tau}\,\mathrm{e}^{\frac{-k\tau}{\gamma}} - \frac{\gamma}{2k\tau}\,\mathrm{e}^{\frac{-2k\tau}{\gamma}} - \frac{3\gamma}{2k\tau}\right) \tag{4.13}$$

Here, a critical time τ_c can be defined as $\tau_c = \gamma/k = 1/2\pi f_c$. For times $\tau \ll \tau_c$, which for the video-based analysis is almost always given, the Allan deviation (the square root of the Allan variance) reduces to[22]

$$\sigma_A(\tau) = \frac{1}{k}\sqrt{\frac{2k_BT\gamma}{\tau}} \tag{4.14}$$

Fitting $\sigma_A(\tau)/\beta$, which is the Allan deviation in camera units, to the data gives us $k\beta$, which is the parameter needed for the force calculation as described by eq. 2.3.

An exemplary Allan fit using the same data as in fig. 4.4 is shown in fig. 4.5, with the fit results shown in table 4.2. Especially the left part of the data with lower τ fits very well. In comparison to fig. 4.4, a counterpart for the deviation for longer times τ can be found as the deviation for very low frequencies. Note however that the detail of the Allan data is logarithmically equally distributed and completely within the same order of magnitude.

To sum up, as Allan variance allows for very precise calibrations without the need to move the bead and as it is directly suitable for low sampling rates, it is the favoured method of calibration. However, calculation is rather complex and works offline. In practise, this means that around 5 s of data need to be acquired, whose calculation takes about another 5 s. I also find the concept of Allan variance more illustrative then the other methods of calibration. Not only allows it for precise calibrations, it also immediately shows long-term drift and periodic disturbances at one glance in a way I find easier to understand than the Fourier-based PSD analysis.

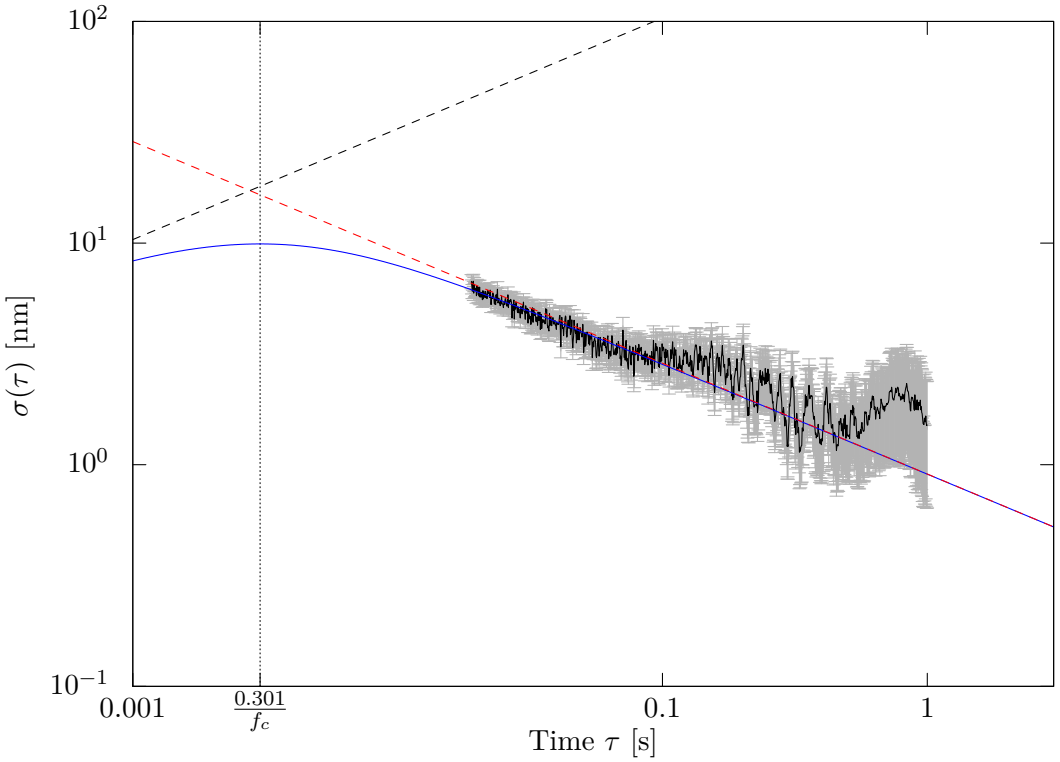

Fig. 4.5.: Exemplary Allan deviation fit. The Allan deviation of the data (converted to real-world units) is shown in black with error bars in grey, the fit is shown in blue and the approximation according to eq. 4.14 is shown in red

5. Measurements and Results

In the past year, video-based axial force measurements have become the norm in our group. In this section, I want to highlight four measurements that were also part of the appended publication, as they are exemplary results showcasing the capabilities of video-based force analysis.

5.1. Interference effects and the bead size

5.1.1. Interference magnitude for different bead sizes

One of the first tests of the video-based force detection was to trap a 3.28 µm bead and slowly approach a Si_3N_4 membrane, recording both the force measurements from the photodetector and the video-based method. In this test, backscattered light based force analysis always shows an interference effect obeying the interference of a standing wave, with constructive interference occuring every $\lambda/2n$ with n being the refraction index of the medium, i.e. water.

Up until now, we though that this was an interference effect on the photodetector, i.e. the backscattered light from the bead and the (much less intense) light backscattered from the membrane interfere there. However, fig. 5.1 shows the same interference effect with comparable intensity of ±1 pN at 900 mW laser power for video-based analysis.

Therefore it must be concluded that the effect is "real" in the sense that it is a standing wave between bead and membrane shifting the position of the optical trap depending on the distance between bead and membrane. They both act as the mirrors of a resonator, albeit with only about 1 % reflectivity.

The aforementioned formula for the interference of a standing wave still holds true. According to it, the interference should occur every 403 nm, whilst we measured a distance between subsequent force maxima of 409 nm.

Beads with 3.05 µm diameter have not been used for backscattered light detection previously since they only reflect about a third of the light compared to 3.28 µm beads.

If our conclusion that the effect is indeed a standing wave induced shifting of the trap position held true, the interference effect should only be a third with this beads.

This is indeed true as illustrated by fig. 5.2. Whilst video-based force analysis shows only minute interference, the interference of the backscattered light based method is off the charts as the signals need to be amplified much more, resulting in more noise and the amplification of the light backscattered from the membrane, creating even more disturbances and oscillation artefacts.

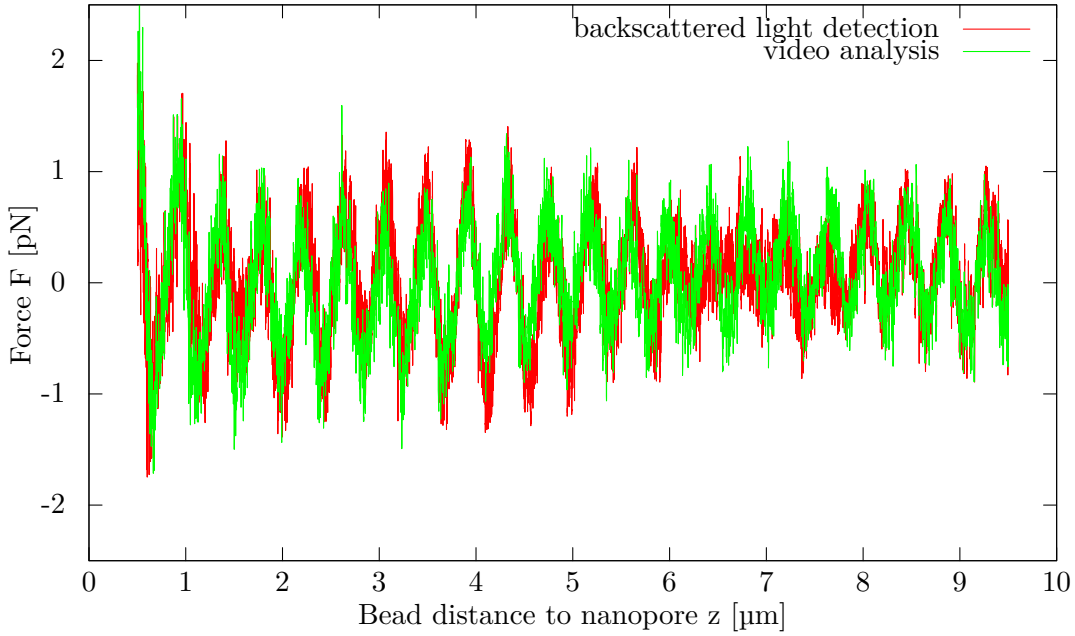

Fig. 5.1.: 3.28 µm bead approaching a membrane, measured with backscattered light detection and video-based analysis

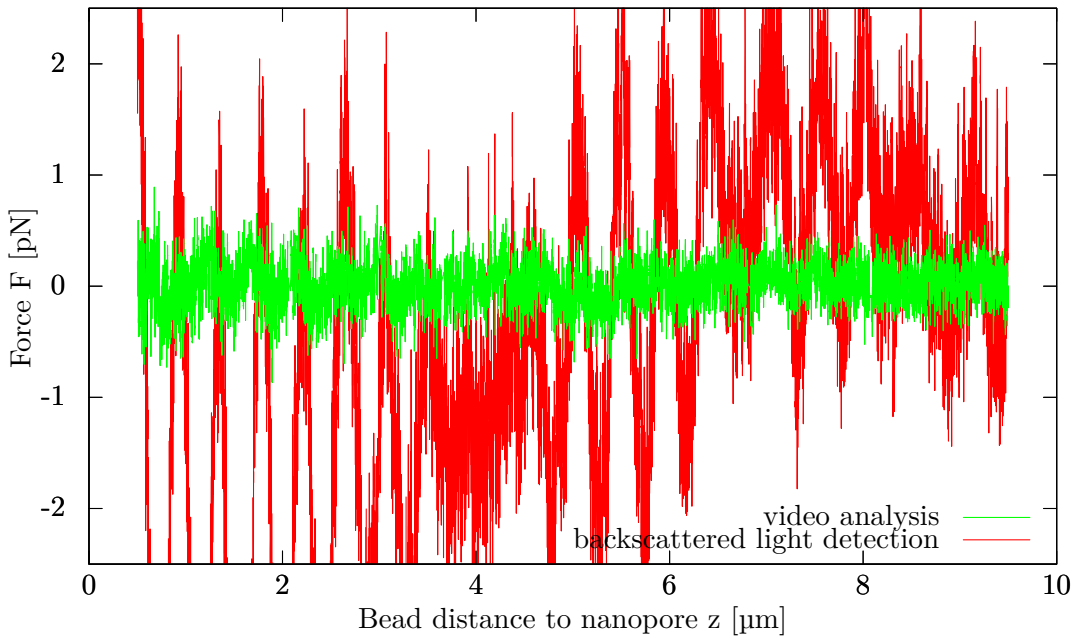

Fig. 5.2.: 3.05 µm bead approaching a membrane, measured with backscattered light detection and video-based analysis

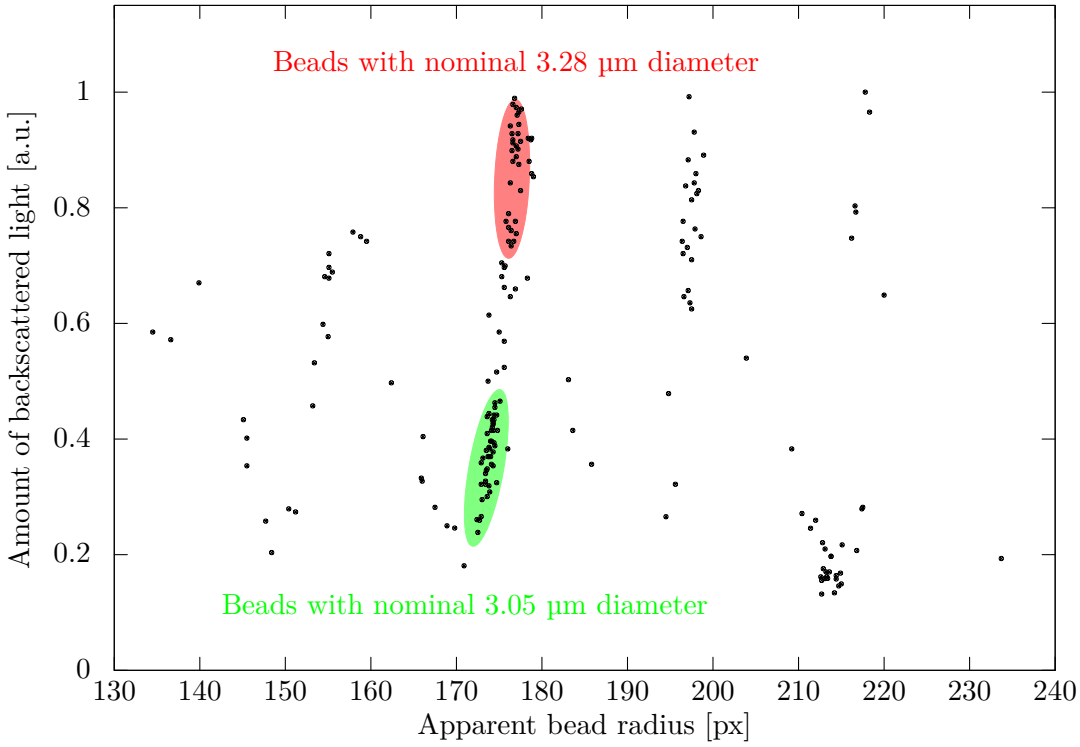

Fig. 5.3.: Dependency of the amount of backscattered light on the apparent bead size

5.1.2. Determination of the optimal bead size

As the quality of force measurements depends on the bead size, one would like to find an optimal size for best results. This bead would reflect as little light as possible, therefore creating only minute interference. It would not be suitable for backscattered light based force analysis, but produce excellent results in video-based analysis.

The reflectivity of a bead can be measured easily with the photodiode for axial backscattered light based force analysis. André Spiering trapped a number of beads with different sizes, using batches of beads with a nominal size of 3.05 µm and 3.28 µm. As the beads were not exactly as large as their nominal size suggests, a wide range of beads could be measured.

Plotting the amount of backscattered light versus the apparent bead size results in fig. 5.3. There seems to be some kind of periodical pattern, a detailed theoretical description of it is available in [24]. Interesting to us are the two marked areas, showing the typical size of beads from the 3.28 µm batch as 176 px to 178 px and the typical size of beads from the 3.05 µm batch as 172 px to 175 px, right next to the minimum at 171 px, which would be an optimal bead size.

Our task for precise measurements is therefore to only use beads with a diameter of 171 px.

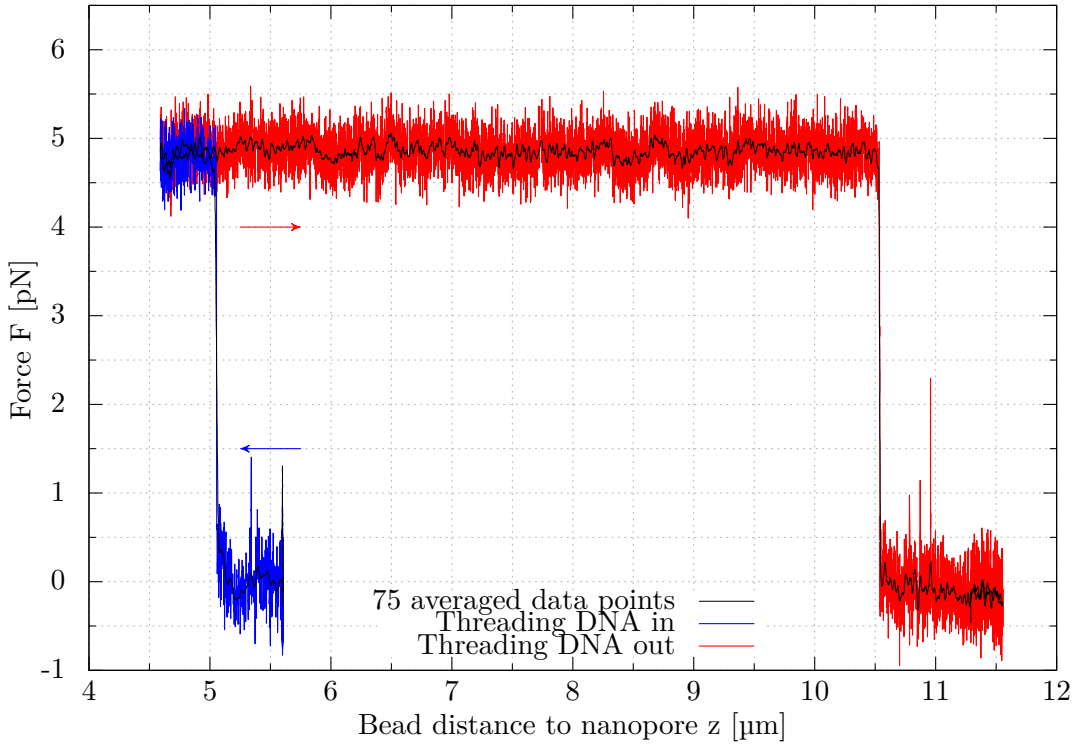

Fig. 5.4.: Controlled translocation of a dsDNA attached to a 3.05 µm bead (apparent radius 171 px) through a SI_3N_4 nanopore (pore diameter 55 nm, applied voltage 50 mV)

5.2. Controlled translocation of DNA through solid state nanopores

Such a 171 px bead was used to measure the force during controlled translocation of a single dsDNA strand through a Si_3N_4 nanopore, as shown in fig. 5.4.

The nanopore has been drilled into a 20 nm thick Si_3N_4 membrane with a Helium ion microscope as described in [25]. The nanopore size was determined to be 55 nm based on the electrical current through the pore. Freshly prepared beads with DNA attached via streptavidin-biotine-binding were introduced into the sample chamber with the mounted membrane. A bead of appropriate size was trapped and navigated in front of the nanopore. With an applied voltage of 50 mV to the trans-chamber, the bead was slowly moved towards the membrane, starting at a distance of 5.60 µm. At 5.05 µm the force suddely increases, meaning the DNA strand has been pulled into the nanopore.

At a distance of 4.59 µm, the movement of the bead is reversed. As it moves further away from the membrane, the force remains constant at 4.9 pN, which is in agreement with typical force values for pores of this size[26,27], with only very slight fluctuations

– the DNA is still inside the nanopore. It is noteworthy that the force fluctuations are in a range of only ±0.5 pN, which further reduces to ±0.2 pN upon averaging 75 data points. There are *no noticeable force oscillations*, showing that interference-free measurements are possible with video-based force analysis and an optimal bead size.

At 10.5 µm distance to the nanopore, the force suddenly drops to zero again, meaning the DNA has been pulled out of the nanopore. As the DNA often sticks to the bead, the full end-to-end distance is not reached.

6. Conclusions

I developed and introduced video-based axial force analysis as a precise alternative to backscattered light based force analysis. In combination with high magnification, this method allows for a more direct measurement of the axial displacement with a resolution of 2.5 nm. It is now used as the main method for axial force detection in our group.

As the drag force calibration method has a number of disadvantages and the calibration via the fitting of a Lorentzian spectrum to the Fourier transformed noise spectrum yields poor results due to the low sampling rate of video-based analysis, I introduced Allan variance as a new method for calibrating force detection. It also allows to analyse drift and periodic disturbances at one glance.

Comparing video-based axial force analysis with the backscattered light approach for different particle sizes shows two things: First, the interference effects measured with the backscattered light method are not artefacts induced on the photodiode but real displacements of the position of the optical trap, caused by a standing wave between bead and membrane/surface.

Secondly, specific bead sizes reflect almost no light and are therefore unsuitable for backscattered light analysis. However, these beads also show no interference effects. As the video-based approach does not rely on the reflectivity of the beads, it allows for the first time for precise and interference-free axial force detection and analysis for optical tweezers.

7. Outlook

The video-based method for axial force analysis is already in use in our day to day measurements in the group. It is a valuable tool for the study of nanopore translocation processes, be it silicon nitride or graphene monolayer pores, pure DNA or DNA with attached ligands.

One of the next possible steps is to integrate video-based radial force analysis. This would be an easy step, as the program already delivers not only the size but also the position of the bead. With some changes to the way the region of interest for the edge detection is handled, we should be able to analyse forces in all three dimensions with just one detector.

Another promising way is the Allan variance. We just topped the edge of the iceberg by using it for force calibration. As other researchers have shown[28], Allan variance offers a whole field of possibilities, especially in the area of noise analysis.

Finally, one might be tempted to reach for faster frame rates with better cameras. As the setup is currently operating near its power limit, the real-time analysis of the data or just of parts of the data whilst streaming the rest of the raw data to disk will prove challenging. Other groups have shown real-time radial force analysis up to 10 000 fps[29], which shows that we are far from the end of the line.

A. Bibliography

[1]S. Knust, A. Spiering, H. Vieker, A. Beyer, A. Gölzhäuser, K. Tönsing, A. Sischka, and D. Anselmetti, "Video-based and interference-free axial force detection and analysis for optical tweezers", Review of Scientific Instruments **83**, 103704 (2012).

[2]J. Eichler and H. J. Eichler, *Laser: Bauformen, Strahlführung, Anwendungen*, 6. Auflage (Springer, 2006).

[3]A. Ashkin, "Acceleration and Trapping of Particles by Radiation Pressure", Physical Review Letters **24**, 156–159 (1970).

[4]A. Ashkin, "Forces of a single-beam gradient laser trap on a dielectric sphere in the ray optics regime", Biophysical Journal **61**, 569–582 (1992).

[5]A. Ashkin, "Optical Levitation by Radiation Pressure", Applied Physics Letters **19**, 283 (1971).

[6]A. Ashkin, J. M. Dziedzic, J. E. Bjorkholm, and S. Chu, "Observation of a single-beam gradient force optical trap for dielectric particles", Opt. Lett. **11**, 288 (1986).

[7]W. Denk and W. W. Webb, "Optical measurement of picometer displacements of transparent microscopic objects.", Applied optics **29**, 2382–91 (1990).

[8]U. F. Keyser, J. van der Does, C. Dekker, and N. H. Dekker, "Optical tweezers for force measurements on DNA in nanopores", Rev. Sci. Instrum. **77**, 105105 (2006).

[9]A. R. Carter, G. M. King, and T. T. Perkins, "Back-scattered detection provides atomic-scale localization precision, stability, and registration in 3D.", Optics express **15**, 13434–45 (2007).

[10]A. Sischka, C. Kleimann, W. Hachmann, M. M. Schafer, I. Seuffert, K. Tönsing, and D. Anselmetti, "Single beam optical tweezers setup with backscattered light detection for three-dimensional measurements on DNA and nanopores", Rev. Sci. Instrum. **79**, 63702 (2008).

[11]J. Crocker, "Methods of Digital Video Microscopy for Colloidal Studies", Journal of Colloid and Interface Science **179**, 298–310 (1996).

[12]G. M. Gibson, J. Leach, S. Keen, A. J. Wright, and M. J. Padgett, "Measuring the accuracy of particle position and force in optical tweezers using high-speed video microscopy", Opt. Express **16**, 14561 (2008).

[13]O. Otto, F. Czerwinski, J. L. Gornall, G. Stober, L. B. Oddershede, R. Seidel, and U. F. Keyser, "Real-time particle tracking at 10,000 fps using optical fiber illumination", Opt. Express **18**, 22722–22733 (2010).

[14]A. Rohrbach and E. H. K. Stelzer, "Three-dimensional position detection of optically trapped dielectric particles", Journal of Applied Physics **91**, 5474 (2002).

[15]P. Christen and R. Jaussi, *Biochemie*, Springer-Lehrbuch (Springer-Verlag, Berlin/Heidelberg, 2005), http://www.springerlink.com/index/10.1007/b137457.

[16]C. Bustamante, J. Marko, E. Siggia, and S. Smith, "Entropic elasticity of lambda-phage DNA", Science **265**, 1599–1600 (1994).

[17]Laser 2000, *Laser und Lichtquellen*, 2011, http://www.laser2000.de/index.php?id=363099.

[18]Allied Vision Tech, *AVT Guppy PRO Technical Manual*, 2012, http://www.alliedvisiontec.com/fileadmin/content/PDF/Products/Technical_Manual/Guppy_PRO/Guppy_PRO_TechMan_V4.0.0_en.pdf.

[19]G. W. C. Kaye and T. H. Laby, *Tables of Physical & Chemical Constants*, 16th Ed. (Kaye & Laby Online Version 1.0, 2005), http://www.kayelaby.npl.co.uk/.

[20]K. Svoboda and S. M. Block, "Biological applications of optical forces.", Annual review of biophysics and biomolecular structure **23**, 247–85 (1994).

[21]J. Happel and H. Brenner, *Low Reynolds number hydrodynamics*, 1st paperb (Martinum Nijhoff Publishers, The Hague, The Netherlands, 1983).

[22]B. M. Lansdorp and O. A. Saleh, "Power spectrum and Allan variance methods for calibrating single-molecule video-tracking instruments.", Rev. Sci. Instrum. **83**, 025115 (2012).

[23]N. Wiener, "Generalized harmonic analysis", Acta Mathematica **55**, 117–258 (1930).

[24]V. Bormuth, A. Jannasch, M. Ander, C. M. van Kats, A. van Blaaderen, J. Howard, and E. Schäffer, "Optical trapping of coated microspheres", Opt. Express **16**, 13831 (2008).

[25]A. Spiering, S. Getfert, A. Sischka, P. Reimann, and D. Anselmetti, "Nanopore translocation dynamics of a single DNA-bound protein.", Nano Lett. **11**, 2978–82 (2011).

[26]S. van Dorp, U. F. Keyser, N. H. Dekker, C. Dekker, and S. G. Lemay, "Origin of the electrophoretic force on DNA in solid-state nanopores", Nat. Phys. **5**, 347–351 (2009).

[27]M. van den Hout, I. D. Vilfan, S. Hage, and N. H. Dekker, "Direct force measurements on double-stranded RNA in solid-state nanopores.", Nano Lett. **10**, 701–7 (2010).

[28]F. Czerwinski, A. C. Richardson, and L. B. Oddershede, "Quantifying noise in optical tweezers by allan variance.", Optics express **17**, 13255–69 (2009).

[29]O. Otto, J. L. Gornall, G. Stober, F. Czerwinski, R. Seidel, and U. F. Keyser, "High-speed video-based tracking of optically trapped colloids", J. Opt. **13**, 44011 (2011).

B. Appended publication

The appended publication was submitted to Review of Scientific Instruments on August 16, 2012 and accepted on September 18, 2012. I am the corresponding author for this work, implemented the video-based analysis as described in greater detail in this thesis, and did all the experiments except for the measurement of the dependency of the amount of backscattered light on the apparent bead radius, which was performed by André Spiering as noted before. I prepared figures 2–4, typeset the manuscript and wrote sections II–IV, V-A and VII and collaborated on the remaining sections of the draft with André Spiering and Andy Sischka.

AIP | Review of Scientific Instruments

Video-based and interference-free axial force detection and analysis for optical tweezers

Sebastian Knust, Andre Spiering, Henning Vieker, André Beyer, Armin Gölzhäuser et al.

Citation: Rev. Sci. Instrum. **83**, 103704 (2012); doi: 10.1063/1.4757397
View online: http://dx.doi.org/10.1063/1.4757397
View Table of Contents: http://rsi.aip.org/resource/1/RSINAK/v83/i10
Published by the American Institute of Physics.

Video-based and interference-free axial force detection and analysis for optical tweezers

Sebastian Knust,[1,a)] Andre Spiering,[1] Henning Vieker,[2] André Beyer,[2] Armin Gölzhäuser,[2] Katja Tönsing,[1] Andy Sischka,[1] and Dario Anselmetti[1]
[1]*Experimental Biophysics & Applied Nanoscience, Faculty of Physics, Bielefeld University, 33615 Bielefeld, Germany*
[2]*Physics of Supramolecular Systems, Faculty of Physics, Bielefeld University, 33615 Bielefeld, Germany*

(Received 16 August 2012; accepted 18 September 2012; published online 15 October 2012)

For measuring the minute forces exerted on single molecules during controlled translocation through nanopores with sub-piconewton precision, we have developed a video-based axial force detection and analysis system for optical tweezers. Since our detection system is equipped with a standard and versatile CCD video camera with a limited bandwidth offering operation at moderate light illumination with minimal sample heating, we integrated Allan variance analysis for trap stiffness calibration. Upon manipulating a microbead in the vicinity of a weakly reflecting surface with simultaneous axial force detection, interference effects have to be considered and minimized. We measured and analyzed the backscattering light properties of polystyrene and silica microbeads with different diameters and propose distinct and optimized experimental configurations (microbead material and diameter) for minimal light backscattering and virtually interference-free microbead position detection. As a proof of principle, we investigated the nanopore threading forces of a single dsDNA strand attached to a microbead with an overall force resolution of ±0.5 pN at a sample rate of 123 Hz. © *2012 American Institute of Physics*. [http://dx.doi.org/10.1063/1.4757397]

I. INTRODUCTION

The contactless manipulation and measurement of dielectric microparticles with sub-piconewton force resolution[1] is a unique feature of optical tweezers.[2] To quantify these external forces, the position of the trapped particle has to be determined with both high spatial and temporal resolution preferably in lateral (x and y) and axial (z) directions.[3] For lateral force measurements, this can be achieved by collecting the forward or backscattered light of the trapped particle and projecting it onto a position sensitive detector, such as a quadrant[4] or linear[5] photo detector. Force measurement in z-direction basically requires an intensity detection of the forward or backscattered light coming from the trapped object.[6–8]

To collect the forward scattered light, a condenser objective needs to be confocally adjusted to the trapping objective which limits the space between the two lenses and reduces the versatility of the setup.[9] To overcome this limitation, backscattered light detection can be utilized;[6,7] however, when operating this system in the vicinity of optical interfaces, disturbing force interference effects occur that can only be partially suppressed with an improved optical setup.[7]

Alternatively, video-based image analysis of the trapped object can be utilized for position detection and tracking but sometimes lacks temporal resolution, which can be overcome by strongly increasing the illumination intensity[10] to reduce exposure time or by limiting the active pixel area to boost data output.

In this paper, we introduce a video-based force detection setup based on a standard CCD camera with a limited bandwidth operating at moderate light illumination with minimal sample heating, which delivers high force resolution in axial direction. Force calibration of the optical trap is realized by Allan variance (AV) algorithm[11] and tested with polystyrene (PS) and silica microparticles. As a proof of concept, we analyzed the controlled DNA translocation through a solid-state nanopore (NP) inside a membrane. Moreover, we investigated the axial force response signal of different microparticles when navigating these particles into the vicinity of this weakly reflecting surface. These results are compared to our previous measurements based on backscattered light detection. Furthermore, we show that only video analysis in combination with certain microbead sizes will provide a force signal completely devoid of any force interference effects, for which the backscattered light detection method can only deliver a very limited force signal response.

II. OPTICAL TWEEZERS SETUP

The optical tweezers system is adapted from our previously described backscattered light detection setup[7,12] (Fig. 1).

Briefly, the P-polarized beam (filled line in Fig. 1(a)) of a 1 W, 1064 nm Nd:YAG-laser (LCS-DTL-322, Laser 2000, Germany) is passing a 1064 nm longpass filter, a polarizing beam splitter cube (Linos, Germany) and is expanded to a diameter of about 9 mm for overfilling the back aperture of the water immersion trapping objective (5.7 mm diameter) with a numerical aperture of 1.2 (UPL-APO60W/IR, Olympus, Japan). Arranged in front, a quarter wave plate

a)Author to whom correspondence should be addressed. Electronic mail: sknust@physik.uni-bielefeld.de.

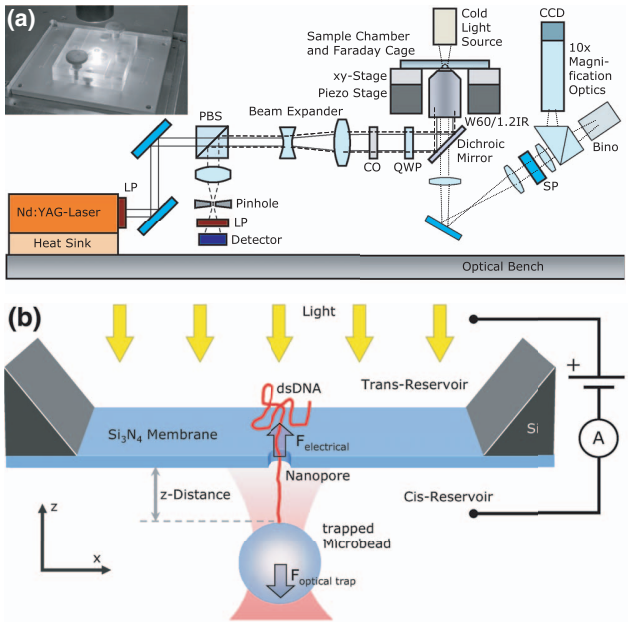

FIG. 1. (a) Quantitative single beam optical tweezers setup with both backscattered light and video-based force detection. Abbreviations: LP: 1064 nm longpass filter; PBS: polarizing beam splitter cube; SP: shortpass filter for visual light; QWP: quarter wave plate; CO: central obstruction filter. Dashed lines indicate backscattered laser light, whereas visible light is indicated as dotted lines. (Inset) Image of the illuminated sample chamber inside the faraday cage (electrical contacting not shown). (b) Detailed view of the Si_3N_4 membrane with nanopore and threaded DNA attached to a trapped microbead. Electrical contacting is shown schematically.

(RM-1/4-1046, Newport, CA) turns the linearly polarized into right-circularly polarized light, which is afterwards reflected by a dichroic mirror (TFP 1064 nm/56°, Laseroptik, Germany). Backscattered laser light (dashed line in Fig. 1(a)) from the trapped particle (now left-circularly polarized) is collected by the trapping objective that turns it into a parallel light beam. The quarter wave plate changes it into linearly S-polarized light and after passing the beam expander, the beam is reflected by the polarizing beam splitter cube and confocally projected (aspherical lens $f = 10$ mm, pinhole diameter of 15 μm) through a 1064 nm longpass filter onto a photo detector (SD172-11-21-221, Laser Components, Germany).

A central obstruction filter (CO in Fig. 1(a)) placed in the incoming laser light path not only forms a ring-like laser beam profile inducing a higher force constant in z-direction, but considerably reduces disturbing backscattered light from optical interfaces such as a low reflective membrane when performing force measurements on trapped microspheres close to that interface.[7]

For eye and camera safety, two KG5 short pass filters are placed in the path of the visible light (dotted line in Fig. 1(a)).

The custom-built sample chamber encloses a silicon chip with a Si_3N_4 membrane containing a single nanopore.[12] The chamber on each side of that pore is connected to its respective reservoir where a transmembrane voltage can be applied and functionalized microbeads are introduced that can be individually trapped and navigated to the nanopore (Fig. 1(b)). Each reservoir is electrically contacted by an agarose gel and cyanoferrat salt bridge with an embedded platinum wire connected to an Axopatch 200B amplifier (Molecular Devices, CA).

The sample chamber can be coarse-adjusted by a micrometer-precise manual stage and additionally position controlled with nanometer precision by a piezo stage (P-517.3CD, Physik Instrumente, Germany) during all experiments. For illumination, we use a high-power cold light source (KL 2500 LED, Schott, Germany) with an output of 1000 lm at the end of the glass fiber that is installed about 2 cm above the top of the sample chamber (inset of Fig. 1(a)).

III. VIDEO-BASED FORCE ANALYSIS

For video-based force analysis we integrated a CCD camera (Guppy Pro F-031 monochrome, Allied Vision Technologies, Germany) and a custom-built post-magnification with a factor of 10. The focal plane of the camera was aligned to the focal plane of the trap by adjusting the distance until a trapped bead was imaged sharply. Focal imprecision only results in a slightly blurry image of the bead which is not disturbing the analysis significantly, making the analysis robust and reliable. The camera delivers 123 frames per second at a resolution of 492 × 492 pixels (5.6 μm pixel size) with 14-bit gray scale through Firewire-B connection. Image analysis is completely software based on a CPU with six cores and twelve parallel threads.

Video-based force analysis and particle tracking in lateral direction has been shown in previous papers.[10,13,14] Usually, these methods involve high speed cameras with limited lateral resolution. Since we want to analyze the axial force acting on a trapped bead in front of a Si_3N_4 membrane, we need to continuously monitor the apparent size of the video-imaged bead. For this purpose, high lateral resolution of the bead's image is mandatory, which is achieved by using a post-magnification in front of the camera resulting in a lateral scale of approximately 9 nm per pixel.

For all measurements, the apparent size of a bead needs to be precisely determined, which is done by searching for specific edges in the single image, as illustrated in Fig. 2(a). First, we manually select a circular region of interest. Then, the strongest falling and rising edges along 360 circular spokes in this circle are determined. If both exceed a certain threshold value and are in the correct relation to each other (which means the falling edge is closer to the bead's center than the rising edge), the middle position between these two edges is calculated (Fig. 2(b)), and a circle is fitted through those points. On demand, to compensate transversal drift, the position of this circle can be used to auto track the region of interest by aligning its center to the center of the circle.

The edge detection is done by utilizing the built-in *IMAQ Spoke 3* function of the NI Vision Development Module 2009 for LabView (National Instruments, TX). We empirically determined the optimal parameters with respect to execution time and noise to be: Kernel Size: 35; Width: 9; Minimum Edge Strength: 0.00; Interpolation Type: Bilinear Fixed; Data Processing Method: Average. As the minimum edge strength is set to zero, the step of comparing the edge strength to the threshold is obsolete. However, it might improve the results

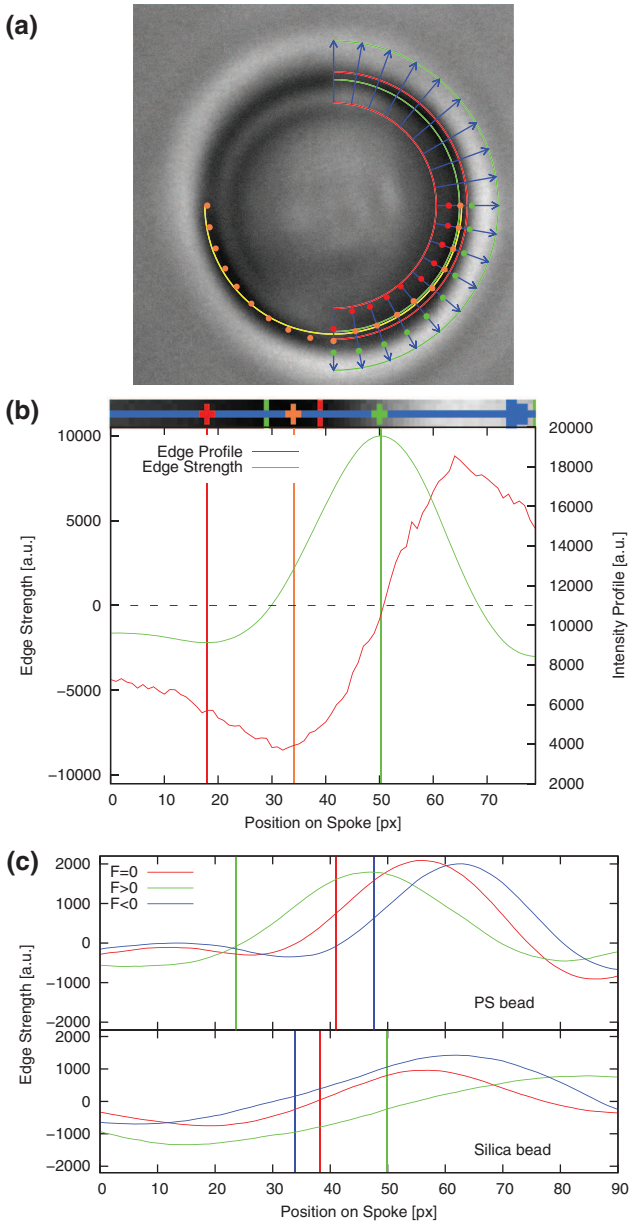

FIG. 2. (a) Still frame of a PS bead with manually selected circular region of interest for falling (red) and rising (green) edge with search spokes (blue). The red and green dots are the recognized falling and rising edges. The orange dots are the resulting mid-points between the two edges, through which the yellow circle is fitted. For clarity, only every tenth spoke with corresponding edges is shown. (b) (Top) Extract of a still frame with region of interest boundaries, spoke, and detected edges. (Bottom) Raw edge profile (red) and calculated edge strength (green) of that profile with marked falling (red) and rising (green) edge position. (c) Edge strength along one spoke for PS (top) and silica (bottom) beads without applied force (red) and with applied positive (green) and negative (blue) force. The middle position between the rising and falling edge is marked by a vertical line.

under different lighting conditions. The LabView source file containing the size detection is available in the supplementary material.[21]

By analyzing six frames in parallel, we are able to analyze the camera images with the maximum frame rate of 123 frames per second in real-time.

IV. FORCE CALIBRATION

Basic force calibration of the optical tweezers was conducted using the drag force via Stokes' law by moving the piezo in z-direction with a specified velocity. As a result, we found that the apparent size of a PS bead decreases, whereas in contrast, the size of a silica bead increases when a positive external force is applied and the bead is axially deflected inside the optical trap (Fig. 2(c)).

It is worth noting that the apparent size of the bead grows minimally when increasing the distance between bead and membrane due to a slight change in the lighting situation. This linear effect is in the order of 0.2% relative size change across the whole piezo stage z-range of 20 μm and can easily be eliminated by a linear correction factor.

The force can now be derived from the calculated apparent radius r as

$$F = k\Delta z = k\beta \times \left(\frac{r}{r_{zf}(z)} - 1\right). \tag{1}$$

Here, k is the force constant of the optical trap, β is a conversion factor between relative radius change and bead deflection Δz, and $r_{zf}(z)$ is the apparent radius of the bead at zero force.

Because $r_{zf}(z)$ depends on the piezo position as described above, a linear interpolation based on two reference zero force measurements at different piezo positions is included.

For all used PS beads, the conversion factor β is in the order of 10 μm, meaning a 0.025% change of the radius (which is our detection limit) corresponds to a 2.5 nm axial displacement of the bead.

The drag force method can be applied to video-based force analysis, but it yields a calibration error of about 10%. Fitting a Lorentzian function to the thermal noise spectrum is not suitable here due to the rather low sampling rate of the video signal, thus making an alternative method mandatory.

Allan variance is such a method perfectly qualified for low frequency signals.[11] It is defined as half the variance of the averaged difference between two consecutive local averaged position samples:

$$\sigma^2(\tau) = \frac{1}{2}\langle(\bar{x}_{\tau,j+1} - \bar{x}_{\tau,j})^2\rangle,$$
$$\bar{x}_{\tau,j} = \frac{1}{\tau}\int_{\tau(j-0.5)}^{\tau(j+0.5)} dt\, x(t). \tag{2}$$

Here, $x(t)$ is the bead position, j an integer, and τ the timescale of both the time between consecutive samples and the time over which each sample is being averaged.

AV was primarily used to quantify the performance of generic measurement systems and to quantify the influences of noise and drift;[15] however, it also yields the analytical expression of our trapped bead as a damped harmonic oscillator[11] as

$$\sigma^2_{\text{bead}}(\tau) = \frac{2k_BT\gamma}{k^2\tau} \times \left(1 + \frac{2\gamma}{k\tau}\exp\left[\frac{-k\tau}{\gamma}\right] - \frac{\gamma}{2k\tau}\exp\left[\frac{-2k\tau}{\gamma}\right] - \frac{3\gamma}{2k\tau}\right). \tag{3}$$

Here, $\gamma = 6\pi\eta r$ is the friction coefficient of a microbead with radius r inside a fluid with viscosity η. For the thermal limit $\tau \gg \tau_c$ (with the time-constant $\tau_c = \gamma/k$), the Allan *deviation* $\sigma_z(\tau)$ of the displacement of a trapped bead reduces to

$$\sigma_z(\tau) = \frac{1}{k}\sqrt{\frac{2k_BT\gamma}{\tau}}, \tag{4}$$

and the force resolution $\sigma_F(\tau) = k\sigma_z(\tau)$ becomes independent of the force constant k.[15]

Initially, our recorded video data are in units of relative bead size change with unknown conversion factor β in units of displacement. Fitting $\sigma_z(\tau)/\beta$ (with $\sigma_z(\tau)$ given by Eq. (4)) to the AV of our displacement data delivers the product $k\beta$—the parameter needed for Eq. (1). In summary, when an external force is acting on the trapped bead the parameter $k\beta$ directly converts the change of the bead size into force. In contrast to the drag force method, the results of this calibration procedure are not accessible in real time but directly after several seconds of data acquisition and analysis. However, because the bead remains in the same position during the AV calibration, this method significantly reduces the possibility to trap dirt particles and suppresses drag force calibration difficulties that may occur when the mobility of the bead in z-direction inside the sample chamber is limited.

To calculate the force constant k separately, the displacement conversion factor β needs to be determined. This is done by immobilizing a bead on the membrane or the sample chamber bottom, moving the bead with the piezo in z-direction through the center of the optical trap that has been switched off, and recording the relative size change $(r(z)/r_{zf}) - 1$. The value of β can then be determined from the slope of a linear fit of the piezo position z versus the relative size change of the bead. β can now be utilized for all trapped beads of the same apparent radius, material, and lighting condition.

V. EXPERIMENTAL PROCEDURE

We use monodisperse streptavidin-coated PS beads (3.05 μm and 3.28 μm nominal diameter, concentration of 0.5% w/v; Spherotech, IL) that were diluted by a factor of 1:2000 in NP-buffer (20 mM KCl and 2 mM Tris/HCl at *p*H 8.0) and streptavidin-coated silica beads (3 μm nominal diameter, concentration of 2.5% w/v; Spherotech, IL).

Calibration and all experiments were carried out at 21 °C. Temperature control with an IR camera revealed an ambient sample chamber temperature of 25 °C due to intense lighting of the silicon chip. With these conditions, we are able to achieve an AV calibration accuracy of ±5%.

For controlled DNA translocation through a NP, Lambda-DNA molecules (16.4 μm contour length; Roche Diagnostics, Germany) were multi-biotinylized at one end and individually attached to a 3.05 μm PS bead.[12] Then, DNA-bead constructs were suspended in NP-buffer, introduced into the sample chamber, trapped, and navigated underneath the NP (Fig. 1(b)).

VI. RESULTS AND DISCUSSION

A. Allan variance calibration

Because various sizes of beads consisting of PS and silica yield qualitatively similar AV graphs, we discuss our results of an exemplary AV graph of a 3.05 μm PS bead trapped with a laser output power of 250 mW (green line in Fig. 3, black error bars). The conversion factor β has been determined as (9.21 ± 0.04) μm. The left ordinate in Fig. 3 displays AV data in nm, and the right ordinate shows the respective relative size change of the trapped bead in percent.

The main section of our data ($\tau < 1$ s) matches very well the theoretical model for the overdamped bead in a harmonic oscillator (Eq. (3), and blue line in Fig. 3), whereas for times larger than several seconds, drift effects deviate the AV results from that model. As both Eq. (3) and the thermal limit (Eq. (4), and red dashed line in Fig. 3) do not deviate within range of our data, a fit of the AV results to the thermal limit is feasible.

Fitting $\sigma_z(\tau)/\beta$ to our data yields the value of $k\beta$ as to be (106.8 ± 03) pN, which means a change of the apparent bead size of 0.025% corresponds to a force of 27 fN.

With the predetermined value of β, we calculated k to be (11.60 ± 0.02) pN μm^{-1} (that matches our previous results[12] very well) and the time-constant as $\tau_c = \gamma/k = (2.20 \pm 0.01)$ ms.

B. The influence of bead size on the interference

Before the implementation of video analysis, backscattered light detection offered the most precise axial force measurements when approaching a weakly reflective optical interface (e.g., a membrane with a NP) because the combination of confocal and spatial filtering by the CO (Fig. 1(a)) delivers a force signal that is only weakly affected by disturbing interference artifacts.[6,7,16] Thus, it is inevitable to compete the backscatter method against video analysis with regard to the interference effect. For this purpose, a 3.28 μm PS bead (it delivers a sufficient amount of backscattered light[7]) was trapped, calibrated with both detection methods, and approached with a velocity of 200 nm s^{-1} to the 20 nm thin Si_3N_4 membrane, while the force was recorded simultaneously (Fig. 4(a)).

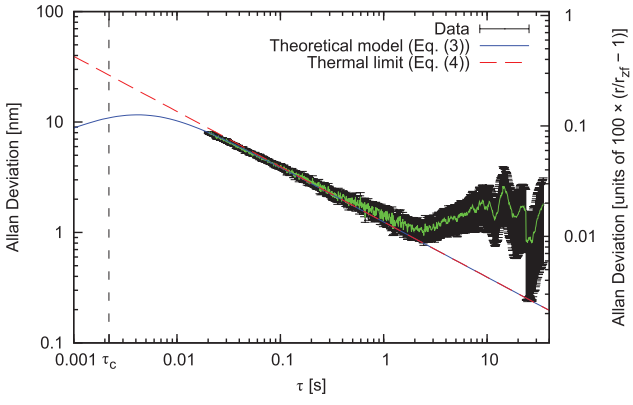

FIG. 3. Exemplary Allan deviation analysis of a trapped 3.05 μm PS bead at 250 mW laser power.

Interestingly, *both* force signals display an almost identical force oscillation of up to ±1 pN (at 900 mW laser output power). This led us to the conclusion that this phenomenon is not an artifact induced on the photo detector where backscattered light from the trapped bead and (much less) backscattered light from the membrane interfere. Instead, the source of this effect is only located between bead and membrane and can be considered as a standing wave excited by laser light which is backscattered from the membrane and backreflected again from the bead. Bead and membrane can be considered as the "mirrors" of an optical resonator, although their reflectivity is only 0.75% and 1%, respectively. The wave obeys the resonator condition for constructive interference ($j\lambda/2n_{\mathrm{w}}$, where n_{w} is the refractive index of water) and modulates the position of the trapped bead with respect to the optical trap when varying the distance between bead and membrane—a modulation that both detection methods cannot discriminate from a real external force acting on the bead and deflecting it inside the trap.

The theoretical length for this resonator exciting constructive interference is $j \times 403$ nm, matching our measured length of 409 nm very well (which is the distance between two consecutive force oscillation maxima). The magnitude of the force oscillation depends linearly on the laser power, which is inferred by the fact that the position modulation in terms of nanometer is independent of the laser power, and has an amplitude of up to ±24 nm for a 3.28 μm PS bead.

In contrast, a trapped 3.05 μm PS bead exhibits a considerably different behavior since it delivers only about a third of the amount of backscattered light a 3.28 μm bead does. Consequently, the resonator's performance declines by a factor of three, and so do the standing wave and the position modulation of the trapped bead as well. As a result, the oscillation of the force signal measured with video analysis has been diminished to ±0.3 pN or less (Fig. 4(b)), yielding a very good force signal displaying almost only Brownian noise.

Because of the extremely low amount of backscattered light from the bead, the photo detector's signal needs to be amplified by a factor of three to maintain its force sensitivity, making the detector more susceptible for backscattered light from the membrane too, since the combination of confocal filtering and the CO can only suppress that backscattered light to a certain amount. Therefore, this force signal is even more affected by that disturbance and exhibits a strong oscillating force artifact of more than ±2 pN.

As the real size of each trapped bead deviates from its nominal value of 3.05 or 3.28 μm, a multitude of bead sizes were examined, each with regard to its apparent radius and the respective amount of backscattered light. Figure 4(c) contains two data point clusters attributed to the batch of the smaller (with a radius between 172 and 175 pixels) and larger beads (with a radius between 176 and 178 pixels). Their corresponding amount of backscattered light extends from 0.2 to 0.5 and from 0.7 to 1.0 arbitrary units for 3.05 μm and 3.28 μm beads, respectively.

The sizes of several beads deviate more significantly from their nominal value, giving us the opportunity to examine a large range of different sizes revealing a rather complex dependency between bead size and amount of backscattered

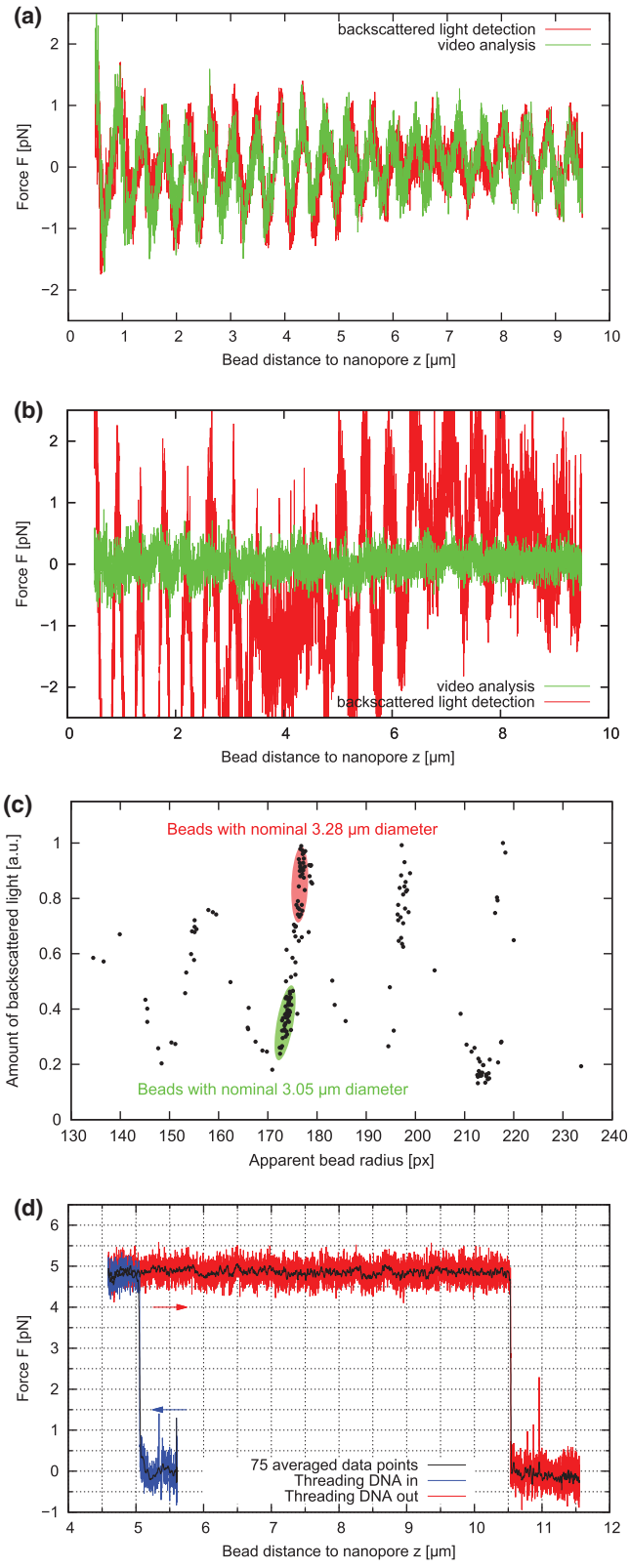

FIG. 4. (a) A 3.28 μm bead approaches the membrane, measured both with backscattered light detection and video analysis. (b) A 3.05 μm bead approaches the membrane, measured both with backscattered light detection and video analysis. (c) Graph showing the dependency of the amount of backscattered light on the apparent bead size. (d) Controlled dsDNA threading with 3.05 μm bead (55 nm pore diameter, applied voltage 50 mV).

light that has been described elsewhere.[17] Extrapolating Fig. 4(c) leads to an optimal PS bead size of 171 pixels corresponding to approximately 3.01 μm.

C. Force measurements during DNA threading

As an appropriate proof of principle, we have measured the small force during a controlled translocation of a single dsDNA strand through a solid state NP with a diameter of 55 nm inside a 20 nm Si_3N_4 membrane that has been drilled as describe before[18] and mounted into the sample chamber. We have introduced freshly prepared bead-DNA constructs into the sample chamber and selected a bead with an apparent radius of 171 pixels, which as shown above is the optimal bead size. Figure 4(d) shows the results of a controlled single-DNA threading event into the NP, when applying a positive voltage of 50 mV to the trans-chamber, before the DNA was completely pulled out of the pore by retracting the bead. While the DNA is inside the pore we have measured an end-to-end distance of this DNA fragment of 10.5 μm and a very constant force signal of 4.9 pN, which is in agreement with force values for large pores.[19,20] Since the DNA often sticks to the bead, the apparent contour length decreases. Force fluctuations at a sample rate of 123 data points per second were in the range of not more than $\pm$0.5 pN, whereupon averaging of 75 data points led to extremely low variations of less than $\pm$0.2 pN with no noticeable force oscillations anymore.

VII. SUMMARY AND CONCLUSION

We presented precise video-based axial force analysis via bead size detection for optical tweezers, which in combination with high magnification allows for an axial displacement resolution of 2.5 nm.

Allan variance was introduced as an alternative force calibration method where fitting a Lorentzian function to the thermal noise spectrum is not possible due to low sampling rates.

The comparison between video-based axial force measurements and backscattered light detection measurements in the vicinity of a weakly reflecting surface led us to the conclusion that interference effects are not artifacts induced on the photo detector but caused by what can be considered a standing wave between the weakly reflecting bead and surface.

We show that beads barely backscattering light exhibit no measurable interference effect in the vicinity of an optical interface. This allows interference-free axial force measurements with the video-based method.

As an exemplary result, we achieved a virtually interference-free axial force resolution of $\pm$0.5 pN at a sample rate of 123 Hz when threading a single dsDNA molecule into a nanopore.

ACKNOWLEDGMENTS

We gratefully acknowledge helpful discussions with Fabian Czerwinski, Thomas Huser, Zachary J. Smith, Matthias Rief, Cees Dekker, Ulrich F. Keyser, and Gautam Soni. We thank Christoph Pelargus, Karsten Rott, Wiebke Hachmann, and Helene Schellenberg for technical support. This work was financially supported by the Collaborative Research Center SFB 613 from the Deutsche Forschungsgemeinschaft (DFG).

[1] J. R. Moffitt, Y. R. Chemla, S. B. Smith, and C. Bustamante, Annu. Rev. Biochem. **77**, 205 (2008).
[2] A. Ashkin, J. M. Dziedzic, J. E. Bjorkholm, and S. Chu, Opt. Lett. **11**, 288 (1986).
[3] K. C. Neuman and S. M. Block, Rev. Sci. Instrum. **75**, 2787 (2004).
[4] F. Gittes and C. F. Schmidt, Opt. Lett. **23**, 7 (1998).
[5] J. Huisstede, K. van der Werf, M. Bennink, and V. Subramaniam, Opt. Express **13**, 1113 (2005).
[6] U. F. Keyser, J. van der Does, C. Dekker, and N. H. Dekker, Rev. Sci. Instrum. **77**, 105105 (2006).
[7] A. Sischka, C. Kleimann, W. Hachmann, M. M. Schafer, I. Seuffert, K. Tönsing, and D. Anselmetti, Rev. Sci. Instrum. **79**, 63702 (2008).
[8] C. Deufel and M. D. Wang, Biophys. J. **90**, 657 (2006).
[9] M. J. Lang, C. L. Asbury, J. W. Shaevitz, and S. M. Block, Biophys. J. **83**, 491 (2002).
[10] O. Otto, F. Czerwinski, J. L. Gornall, G. Stober, L. B. Oddershede, R. Seidel, and U. F. Keyser, Opt. Express **18**, 22722 (2010).
[11] B. M. Lansdorp and O. A. Saleh, Rev. Sci. Instrum. **83**, 025115 (2012).
[12] A. Sischka, A. Spiering, M. Khaksar, M. Laxa, J. König, K.-J. Dietz, and D. Anselmetti, J. Phys.: Condens. Matter **22**, 454121 (2010).
[13] O. Otto, J. L. Gornall, G. Stober, F. Czerwinski, R. Seidel, and U. F. Keyser, J. Opt. **13**, 44011 (2011).
[14] O. Otto, C. Gutsche, F. Kremer, and U. F. Keyser, Rev. Sci. Instrum. **79**, 23710 (2008).
[15] G. M. Gibson, J. Leach, S. Keen, A. J. Wright, and M. J. Padgett, Opt. Express **16**, 14561 (2008).
[16] A. Jonáš, P. Zemánek, and E.-L. Florin, Opt. Lett. **26**, 1466 (2001).
[17] V. Bormuth, A. Jannasch, M. Ander, C. M. van Kats, A. van Blaaderen, J. Howard, and E. Schäffer, Opt. Express **16**, 13831 (2008).
[18] A. Spiering, S. Getfert, A. Sischka, P. Reimann, and D. Anselmetti, Nano Lett. **11**, 2978 (2011).
[19] S. van Dorp, U. F. Keyser, N. H. Dekker, C. Dekker, and S. G. Lemay, Nat. Phys. **5**, 347 (2009).
[20] M. van den Hout, I. D. Vilfan, S. Hage, and N. H. Dekker, Nano Lett. **10**, 701 (2010).
[21] See supplementary material at http://dx.doi.org/10.1063/1.4757397 for the LabView source file containing the size detection.

C. Declaration of own work

I hereby declare that this thesis is my own work, with all assistance acknowledged. It is submitted for the Degree of *Bachelor of Science* at the Bielefeld University and has not been submitted before in any other university.

Ich erkläre hiermit, dass ich diese Arbeit eigenständig und nur mit den angegebenen Hilfsmitteln verfasst habe. Diese Arbeit dient zum Erlangen des Grades *Bachelor of Science* an der Universität Bielefeld und wurde zuvor an keiner anderen Hochschule eingereicht.

Bielefeld, _____

_____

Sebastian Knust